INFORMATION TO USERS

This manuscript has been reproduced from the microfilm master. UMI films the text directly from the original or copy submitted. Thus, some thesis and dissertation copies are in typewriter face, while others may be from any type of computer printer.

The quality of this reproduction is dependent upon the quality of the copy submitted. Broken or indistinct print, colored or poor quality illustrations and photographs, print bleedthrough, substandard margins, and improper alignment can adversely affect reproduction.

In the unlikely event that the author did not send UMI a complete manuscript and there are missing pages, these will be noted. Also, if unauthorized copyright material had to be removed, a note will indicate the deletion.

Oversize materials (e.g., maps, drawings, charts) are reproduced by sectioning the original, beginning at the upper left-hand corner and continuing from left to right in equal sections with small overlaps. Each original is also photographed in one exposure and is included in reduced form at the back of the book.

Photographs included in the original manuscript have been reproduced xerographically in this copy. Higher quality 6" x 9" black and white photographic prints are available for any photographs or illustrations appearing in this copy for an additional charge. Contact UMI directly to order.

UMI

A Bell & Howell Information Company
300 North Zeeb Road, Ann Arbor MI 48106-1346 USA
313/761-4700 800/521-0600

NUMERICAL SIMULATIONS OF

PHASE SEPARATION OF DEEPLY QUENCHED MIXTURES

by

NATALIA VLADIMIROVA

A dissertation submitted to the Graduate Faculty in Engineering
in partial fulfillment of the requirements for the degree of
Doctor of Philosophy. The City University of New York

1998

This manuscript has been read and accepted for the Graduate Faculty in Engineering in satisfaction of the dissertation requirement for the degree of Doctor of Philosophy.

9/10/98 — Date

Chair of Examing Committee

9-10-98 — Date

Mumtaz K. Kazimi — Executive Officer

Prof. Reuel Shinnar

Prof. Charles Maldarelli

Prof. George Triantafyllou

Dr. Andrea Malagoli

Supervisory Committee

THE CITY UNIVERSITY OF NEW YORK

Abstract

NUMERICAL SIMULATIONS OF

PHASE SEPARATION OF DEEPLY QUENCHED MIXTURES

by

Natalia Vladimirova

Adviser: Professor Roberto Mauri

In this work the phase separation of deeply quenched mixtures is studied. The theoretical model follows the standard model *H*, where convection and diffusion are coupled via a body force, which depends on the Peclet number α, expressing the ratio of thermal to viscous forces. In the limit of sharp interfaces separating single-phase domains, the coupling term reduces to the capillary force.

For small Peclet numbers, $\alpha < 10^2$, the system forms single-phase domains, which can be drops or filaments depending on the mixture composition, separated from one another by sharp interfaces. These single-phase domains thicken as the system tries to minimize its interfacial area, with the typical domain size R growing in time as $t^{1/3}$, in agreement with theoretical predictions. Phase separation for larger Peclet numbers is characterized by slower change of composition and faster domain growth. In fact, when $\alpha > 10^3$, the typical drop size increases linearly with time, with a growth rate proportional to the ratio between molecular diffusivity and interface thickness, in agreement with the experimental results. In addition, phase separation and domain growth occur simultaneously when the Peclet number is large, while, for

small Peclet numbers, first sharp interfaces appear, and then the single-phase domains start to grow. The composition field within and without these microdomains appears to be non-uniform and time-dependent, even after the formation of sharp interfaces, thereby contradicting the commonly accepted assumption of local equilibrium at the late stage of phase separation.

This theoretical model was validated determining the velocity of a single drop immersed in a phase-separating continuum field with constant concentration gradient, finding that it is proportional to the concentration gradient and inversely proportional to the capillary number. A single drop, immersed in a homogeneous concentration field, it shrinks without moving, if the difference between the initial concentration of the continuum phase and its equilibrium value is negative. In the opposite case the drop grows linearly, consuming material from the surrounding field and moving randomly, propelled by the induced capillary driving force. Two drops, immersed in a continuum field, experience a mutual attraction, induced by the capillary force, which may or may not lead to the drop coalescence, depending on the concentration of continuum phase.

TABLE OF CONTENTS

LIST OF TABLES

LIST OF FIGURES

CHAPTER 1

INTRODUCTION

Phase separation of deeply quenched mixtures can occur either by nucleation (both heterogeneous and homogeneous) or by spinodal decomposition ([1]). The former process describes the relaxation to equilibrium of a metastable system, while the second one is typical of unstable systems. Therefore, nucleation is an activated process, where a free energy barrier has to be overcome in order to form embryos of a critical size, beyond which the new phase grows spontaneously; in most practical cases, suspended impurities or imperfectly wetted surfaces provide the interface on which the growth of the new phase is initiated [2].

Contrary to nucleation, spinodal decomposition occurs spontaneously, without any energy barrier to be overcome, and involves the growth of fluctuations of any amplitude that exceed a critical wavelength [3]. The classical theoretical basis of this process is the Cahn-Hilliard-Cook theory [4], generalizing the previous approach by Van der Waals [5], which was later extended to include non-linear effects [6, 7]. In principle, nucleation and spinodal decomposition are fundamentally different from each other, as metastable systems relax via the activated growth of localized fluctuations of large amplitude, whereas unstable systems do so via the spontaneous growth of long-wavelength fluctuations of any amplitude. However, in practice, the distinc-

tion between the two processes is rather murky [8], as both the critical nucleus size and the critical fluctuation wavelength decrease as the temperature quench increases [9].

Most of the experimental studies on critical binary mixtures [10, 11, 12] have observed that, right after the temperature has crossed that of the miscibility curve, the system starts to separate by diffusion only, leading to the formation of well-defined patches, whose typical size R is described by a power-law time dependence, $R(t) \sim t^n$, where $n \approx 1/3$ when diffusion is the dominant mechanism of material transport, and $n \approx 1$ when hydrodynamic, long-range interactions become important. The shape of these patches appears to depend strongly on the composition of the system: for critical mixtures, they are dendritic, interconnected domains, while for off-critical systems they appear to be spherical drops. Then, in the so-called, "late" stage of coarsening, these patches become large enough that buoyancy dominates surface tension effects, and the mixture separates by gravity [13]. So, during the process of phase separation, the morphology of the system changes dramatically, from that of an unstructured fluid to that of an emulsion, with the phase interfaces being initially non-existing, then very diffuse and, finally, rather sharp [3].

Theoretically, spinodal decomposition in fluids has been described within the framework of the Ginzburg-Landau theory of phase transition [4], showing that during the early stages of the process, initial instabilities grow exponentially, forming, at the end, single-phase microdomains whose size corresponds to the fastest-growing

mode λ_0 of the linear regime [14]. During the late stages of the process, i.e. for times $t > \tau_0 = \lambda_0^2/D$, where D is the molecular diffusivity, the system consists of well-defined patches in which the average concentration is not too far from its equilibrium value [15]. At this point, material transport can occur either by diffusion or by convection. In cases where diffusion is the only transport mechanism, both analytical calculations [16] and dimensional analysis [13] predict a growth law $R(t) \sim t^{1/3}$, due to the Brownian coagulation of droplets. On the other hand, when hydrodynamic interactions among droplets become important, the effect of convective mass flow resulting from surface tension effects cannot be neglected any more. In this case, while dimensional analysis indicates a growth law $R(t) \sim t$ [13, 17], no satisfactory theoretical result has been obtained so far, showing convincingly where the linear growth rate comes from. In two dimension, computer simulations were performed by Farrell and Valls [18], obtaining however a growth rate exponent $n = 0.69$. More recently, Tanaka and Araki [19] showed that the scaling exponent for the domain growth is not universal, and depends on the relative importance of the two relevant transport mechanisms, i.e. hydrodynamic flow and diffusion.

In this work, the evolution of critical binary mixtures is studied. The process is simulated in two dimension, following the so-called model H, in the taxonomy of Halperin and Hohenberg [20], which was originally developed by Kawasaki and coworkers [21]. In this model, the equations of conservation of mass and momentum are coupled via the convective term of the convection-diffusion equation, which is

driven by a composition-dependent body force in the Stokes equation. As noted by Jasnow and Viñals [22], when the system is composed of single-phase domains separated by sharp interfaces, this force incorporates capillary effects, and plays the role of a Marangoni force. After the initial, diffusion-driven stage leads to a non-uniform concentration field, this capillary driving force induces a material flux, which is several orders of magnitude larger than its diffusive counterpart. During the later stages of phase separation this body force is responsible for the strong motion of the single-phase domains that is observed experimentally during phase transition [23]. In particular, as noted by Karpov [24] and Karpov and Oxtoby [25], capillary forces drive the motion of nucleating droplets along a composition gradient, leading to particle clustering and direct coalescence. These aspects of the phenomenon of phase separation are further studied here.

After describing the theoretical model and its numerical implementation in Chapter 2 and 3 respectively, in Chapter 4 we generalize the analysis of Mauri *et al.*[14], studying the diffusion-driven evolution of phase-separating 2D systems, together with the effects a non-uniform, slow quenching. Chapter 5 is devoted to study the influence of convection on phase separating systems, determining why the morphology of a liquid binary mixture is so radically different than that of a polymer solution, as they phase separate. Finally, in Chapter 6, we validate our theoretical model by considering three examples of diffusio-phoresis of drops in two dimensions, that is their motion induced by the concentration gradients of the background field.

First, we study the motion of a single drop immersed in a constant concentration gradient of the continuum phase; then, we follow the motion of a single drop as it phase separates in a uniform background field; finally, the influence of the capillary body force on the coalescence rate of drops is analyzed, simulating the motion of two drops and studying the resulting mutual attractive force. The last Chapter 7 sums up all the relevant results of this research.

CHAPTER 2
THEORETICAL MODEL

Our theoretical model follows the standard model *H*, following the classification of Halperin and Hohenberg [20], which was originally developed by Kawasaki and coworkers [21]. In this model, the equations of conservation of mass and momentum are coupled via a body force, expressing the tendency of the demixing system to minimize its free energy. After discussing the general features of the model *H*, we will introduce few simplifying assumptions, which are needed to make computation less time-consuming, justifying them on physical grounds.

2.1 Gibbs Free Energy and Chemical Potential

Consider a homogeneous mixture of two species A and B with molar fractions x_A and $x_B = 1 - x_A$, respectively, contained in a closed system at temperature T and pressure P. The equilibrium state of this system is such that it minimizes the "coarse-grained" free energy functional, that is the molar Gibbs energy of mixing, Δg_{eq},

$$\Delta g_{eq} = g_{eq} - (g_A x_A + g_B x_B), \tag{2.1}$$

where g_{eq} is the energy of the mixture at equilibrium, while g_A and g_B are the molar free energy of pure species A and B, respectively, at temperature T and pressure P.

The free energy Δg_{eq} is the sum of an ideal part Δg_{id} and a so-called excess part g_{ex}, with

$$\Delta g_{id} = RT[x_A \log x_A + x_B \log x_B]. \tag{2.2}$$

where R is the gas constant, while the excess molar free energy can be expressed as Margules correlation [26],

$$g_{ex} = RTx_A x_B[\Psi_A x_A + \Psi_B x_B]. \tag{2.3}$$

where Ψ_A and Ψ_B are functions of T and P. If A and B have physical properties that are close enough to have $\Psi_A = \Psi_B = \Psi$, the molar free energy (2.3), as well all other two-parameter correlations, such as van Laar's and Wilson's, reduces to the Flory-Huggins expression [27]

$$g_{ex} = RT\Psi x_A x_B. \tag{2.4}$$

This expression is generally derived by considering either the molecular interactions between nearest neighbors [28], or summing all pairwise interactions throughout the whole system [29]. In addition, Eq. (2.4) can be derived from first principles assuming that the $A - A$ and the $B - B$ intermolecular forces are equal to each other and larger than the $A - B$ intermolecular forces, i.e. $F_{AA} = F_{BB} > F_{AB}$, obtaining an expression for Ψ which depends on $(F_{AA} - F_{AB})$ [14]. Systems whose free energy is given by equations (2.1) and (2.2) are generally referred to as regular solutions. In the following, we shall assume that P is fixed, so that the physical state of the mixture at equilibrium depends only on T and x_A.

In order to take into account the effects of spatial inhomogeneities. Cahn and Hilliard [4] applied an original idea by van der Waals [5] and introduced the generalized specific free energy $\tilde{g}$, which for no-flux or periodic boundary conditions is given by the following expression:

$$g = g_{eq} - \frac{1}{2} RTa^2 (\nabla x_A)(\nabla x_B). \tag{2.5}$$

where a represents the typical length of spatial inhomogeneities in the composition. As shown by van der Waals [5], a is proportional to the surface tension between the two phases and for a system near its miscibility curve it is typically of order 0.1 μm [cf. Equation 3.6].

Below a certain critical temperature T_c, corresponding to values $\Psi \geq 2$, the molar free energy given by (2.2) and (2.4) is a double-well potential, and therefore a first-order phase transition will take place. Now, it is well-known that the molar free energy can be written as [26],

$$g_{eq}/RT = \mu_A x_A + \mu_B x_B. \tag{2.6}$$

where μ_A and μ_B denote the chemical potential of species A and B in solution, respectively, i.e.,

$$\mu_A = \frac{1}{RT} \frac{\partial (c g_{eq})}{\partial c_A} \qquad \mu_B = \frac{1}{RT} \frac{\partial (c g_{eq})}{\partial c_B}.$$

Here c_A and c_B denote the mole densities, that is the number of moles per unit volume, of species A and B, respectively, and $c = c_A + c_B$ is the total mole density.

Clearly, $x_A = c_A/c$ and $x_B = c_B/c$. From here we see that the two quantities $\phi = x_A$ and $(\mu_A - \mu_B)$ are thermodynamically conjugated, that is $(\mu_A - \mu_B) = \frac{d(g/RT)}{d\phi}$. This result can be extended [4] defining the generalized chemical potential $\tilde{\mu}$.

$$\tilde{\mu} = \frac{\delta(g/RT)}{\delta\phi}. \tag{2.7}$$

and substituting (2.1)-(2.3) into (2.7) we obtain:

$$\tilde{\mu} = \mu_0 + \log\frac{\phi}{1-\phi} + \Psi_+(1-2\phi) - \Psi_-(1-6\phi+6\phi^2) - a^2\nabla^2\phi. \tag{2.8}$$

where $\mu_0 = (g_B - g_A)/RT$ and

$$\Psi_+ = (\Psi_A + \Psi_B)/2. \qquad \Psi_- = (\Psi_A - \Psi_B)/2.$$

2.2 Continuity Equations

The continuity equation can be written both in terms of number of particles (i.e. moles) and in terms of mass. If all the particles of the system have the same mass, these two approaches are equivalent, as the molar flux can be converted into mass flux by multiplying it by the molar weight, in the same way as the mole density can be converted into mass density. That means that the mole averaged velocity, defined as the ratio between the molar flux and the mole density, is equal to the mass averaged velocity, which, in turn, is defined as the ratio between the mass flux and the mass density. Therefore, in the case of a one-component system, we can talk about velocity v without having to specify whether it is mole- or mass-averaged. In the

same way, in an $A-B$ binary mixture, the velocities of species A and B, $\mathbf{v}_A$ and $\mathbf{v}_B$, respectively, are well-defined quantities which do not require further explanations. Consequently, the usual continuity equations for the molar concentrations c_A and c_B are still valid for the subsystems of particles A and B, i.e.,

$$\frac{\partial c_A}{\partial t} + \nabla \cdot (c_A \mathbf{v}_A) = 0. \tag{2.9}$$

$$\frac{\partial c_B}{\partial t} + \nabla \cdot (c_B \mathbf{v}_B) = 0. \tag{2.10}$$

The difference between the mole averaging and the mass averaging approaches arises only when we write the continuity equation for both species. For example, in the mole averaging case, it is convenient to rewrite Eqs.(2.9) and (2.10) in terms of the total mole density $c = c_A + c_B$ and the mole fraction of one of the species, $x = x_A = c_A/c$, as:

$$\frac{\partial c}{\partial t} + \nabla \cdot (c\mathbf{v}^*) = 0. \tag{2.11}$$

$$c\left(\frac{\partial x}{\partial t} + \mathbf{v}^* \nabla x\right) = -\nabla \cdot \mathbf{j}^*. \tag{2.12}$$

where

$$\mathbf{v}^* = x_A \mathbf{v}_A + x_B \mathbf{v}_B \tag{2.13}$$

is the mole averaged velocity, and

$$\mathbf{j}^* = c\, x_A x_B (\mathbf{v}_A - \mathbf{v}_B) \tag{2.14}$$

is the diffusive molar flux.

In the mass averaging case, we obtain similar equations in terms of the total mass density $\rho = \rho_A + \rho_B$ and the mass fraction of one of the species, $y = y_A = \rho_A/\rho$, with $\rho_A = c_A M_A$ and $\rho_B = c_B M_B$ denoting the mass densities of the individual species, i.e.,

$$\frac{\partial \rho}{\partial t} + \nabla \cdot (\rho \mathbf{v}) = 0, \tag{2.15}$$

$$\rho \left(\frac{\partial y}{\partial t} + \mathbf{v} \nabla y \right) = -\nabla \cdot \mathbf{j}. \tag{2.16}$$

where

$$\mathbf{v} = y_A \mathbf{v}_A + y_B \mathbf{v}_B \tag{2.17}$$

is the mass averaged velocity, and

$$\mathbf{j} = \rho\, y_A y_B (\mathbf{v}_A - \mathbf{v}_B) \tag{2.18}$$

is the diffusive mass flux [30, 31]. Here the mass densities of each individual species are defined as the products between their mole densities and their molar weights, i.e. $\rho_A = c_A M_A$ and $\rho_B = c_B M_B$. Note that when $\rho_A = \rho_B = \rho$ and $M_A = M_B = M$, the mole- and mass-averaged approaches give identical continuity equations.

2.3 Diffusive Flux

For a two-component system, the diffusive mass fluxes of each species A and B are defined as,

$$\mathbf{j}_A = \rho_A (\mathbf{v}_A - \mathbf{v}); \qquad \mathbf{j}_B = \rho_B (\mathbf{v}_B - \mathbf{v}). \tag{2.19}$$

where $\mathbf{v}$ is the mass averaged velocity (2.17). Applying irreversible thermodynamics, this diffusive mass fluxes can be expressed through the following expressions [32, 30].

$$\mathbf{j}_A = -\frac{c}{\rho} M_A M_B D c_A \nabla \mu_A. \tag{2.20}$$

$$\mathbf{j}_B = -\frac{c}{\rho} M_A M_B D c_B \nabla \mu_B. \tag{2.21}$$

where μ_A and μ_B are the chemical potentials of species A and B in solution. Here we have neglected mechanical and thermal driven fluxes, as they are both irrelevant in our case. Note that, since, $\mathbf{j}_A + \mathbf{j}_B = 0$.[cf. Eqs.(2.17) and (2.19)], Eqs. (2.20) and (2.21) satisfy identically the Gibbs-Duhem relation,

$$x_A \nabla \mu_A + x_B \nabla \mu_B = 0. \tag{2.22}$$

Now we intend to determine the expression for the diffusive flux $\mathbf{j}$ appearing in our governing equations. According to Eq. (2.18), $\mathbf{j}$ is proportional to $(\mathbf{v}_A - \mathbf{v}_B)$, where,

$$\mathbf{v}_A - \mathbf{v}_B = \frac{\mathbf{j}_A}{\rho_A} - \frac{\mathbf{j}_B}{\rho_B} = -\frac{c}{\rho} M_A M_B D \nabla \left(\frac{\mu_A}{M_A} - \frac{\mu_B}{M_B} \right). \tag{2.23}$$

Chemical potential gradients can expressed in terms of $\tilde{\mu} = \mu_A - \mu_B$ [cf. Eq. (2.8)] by applying the Gibbs-Duhem relation (2.22), to obtain: $\nabla \mu_A = x_B \nabla \tilde{\mu}$ and $\nabla \mu_B = x_A \nabla \tilde{\mu}$. Finally, substituting these results into Eq. (2.17), and considering that $\rho = c\,(x_A M_A + x_B M_B)$, we conclude:

$$\mathbf{j} = -\rho y_A y_B D \nabla \tilde{\mu}. \tag{2.24}$$

and analogously for the diffusive mole flux.

$$\mathbf{j}^* = -cx_A x_B D \nabla \tilde{\mu}. \tag{2.25}$$

For an ideal mixture, with chemical potential $\tilde{\mu} = \mu^{id} = \log[x_A/x_B]$, we obtain: $\mathbf{j}^* = -cD\nabla x_A$, so that Eq. (2.12) reduces to the usual convection-diffusion equation.

2.4 Navier-Stokes Equation and Capillary Force

To minimize the classical Gibbs free energy (2.1)–(2.4), particles of the same kind tends to accumulate, forming single-phase domains separated by narrow regions with sharp concentration gradients. On the other hand, the additional $a^2(\nabla\phi)^2$ term in the expression for the generalized free energy [cf. Eq. 2.6)] forces the different species to rearrange themselves to minimize the concentration gradients in the system. Macroscopically, the motion within the system is induced by the following body force [20, 18, 22].

$$\mathbf{F}_\phi = \rho\nabla\epsilon = \rho\frac{\partial\epsilon}{\partial\phi}\nabla\phi = \mu\nabla\phi, \tag{2.26}$$

where ϵ is the energy per unit mass, while the chemical potential μ is defined as [31].

$$\mu = \rho RT\left(\frac{\mu_A}{M_A} - \frac{\mu_B}{M_B}\right). \tag{2.27}$$

Included in the Navier-Stokes equation,

$$\rho\left(\frac{\partial\mathbf{v}}{\partial t} + (\mathbf{v}\cdot\nabla)\mathbf{v}\right) = -\nabla p + \nabla\cdot\left\{\eta\left[(\nabla\mathbf{v}) + (\nabla\mathbf{v})^\dagger\right]\right\} + \tag{2.28}$$
$$+\nabla\left\{\left(\zeta - \frac{2}{3}\eta\right)(\nabla\cdot\mathbf{v})\right\} + \rho\mathbf{g} + \mathbf{F}_\phi.$$

this composition dependent force couples it with the diffusion equation (2.16), and induces a convective flux, which is several orders of magnitude larger than the diffusive flux.

When the system is composed of single-phase domains, separated by sharp interfaces, the force (2.26), being proportional to the chemical potential, is driven by the surface energy, and therefore can be interpreted as a capillary force. In fact, as shown by Jasnow and Viñals [22], when the mixture is composed of well-defined single-phase domains separated by a thin interface located at $\mathbf{r} = \mathbf{r}_s$, the body force reduces to the following expression,

$$\mathbf{F}_\sigma(\mathbf{r}) = \left[\hat{\mathbf{n}}\sigma\kappa + (\mathbf{I} - \hat{\mathbf{n}}\hat{\mathbf{n}}) \cdot \nabla\sigma\right] \delta\left[\hat{\mathbf{n}} \cdot (\mathbf{r} - \mathbf{r}_s)\right]. \tag{2.29}$$

where $\hat{\mathbf{n}}$ and κ are the unit vector perpendicular to the interface and the curvature at $\mathbf{r}_s$, respectively. Physically, $\mathbf{F}_\sigma$ tends to minimize the energy stored at the interface, driving, say, A-rich drops towards A-rich region, and therefore enhancing coalescence.

In many numerical approaches to solve moving boundary problems, a so-called color function is defined, which is equal to one in one phase and zero in the other. In the model H, the color function is equal to $\phi/(\Delta\phi)_{eq}$, and therefore it has a clear, unique physical interpretation. On the other hand, in many other approaches the color function has no real physical meaning, and it can be taken as any function

whose integral over a line crossing the interface equals the capillary force (2.29). For example, in Ref. [33] $\mathbf{F}_\phi$ is defined as,

$$\mathbf{F}_\phi = \frac{\sigma\kappa}{(\Delta\phi)_{eq}}\nabla\phi,$$

which is equivalent to assuming that the chemical potential μ in Eq. (2.26) is proportional to the curvature κ. In fact, this is true only in the limit of infinitesimally sharp interface, while, in general, the capillary force $\mathbf{F}_\phi$ is a function of the composition field within the interface region [cf. Eq. (2.26)].

2.5 Governing Equations

The convection of a one-component fluid is usually described in terms of six variables, e.g. the mass density ρ, the mass averaged velocity $\mathbf{v}$, pressure p and temperature T. For a two-component fluid, we have one more variable describing the fluid composition at each location, i.e. the mass fraction y, so that the complete set of equations consists of the mass conservation equation (2.15), the conservation equation for a single species (2.16), the Navier-Stokes equation (2.28), the energy conservation equation and the equation of state. Here we assume that the temperature is constant and therefore we do not need the energy conservation equation. As for the equation of state, in the case of one-component incompressible fluid it usually states that the density is constant, which reduces the number of variables and equations by one, and converts the continuity equation (2.15) into $\nabla \cdot \mathbf{v} = 0$. In the case of a two-

component fluid, the density is a known function of the composition. Substituting $\rho = \rho(y)$ into Equation (2.15) and comparing it with Equation (2.16) we obtain the following equation of state,

$$\nabla \cdot \mathbf{v} = \frac{\rho'(y)}{\rho^2} \nabla \cdot \mathbf{j}. \tag{2.30}$$

where $\rho'(y) = d\rho/dy$. Note that for zero diffusion flux, the system of equations (2.30) and (2.15) can be used to describe the incompressible flow of a variable-density fluid.

$$\frac{\partial \rho}{\partial t} + \mathbf{v} \cdot \nabla \rho = 0, \quad \nabla \cdot \mathbf{v} = 0.$$

The ideal mixture of two incompressible fluids, can give us an example of the function $\rho = \rho(y)$. The mass of each component in the mixture can be expressed both in terms of the specific weights of the pure liquids, ρ_1^o and ρ_2^o, the locally averaged density ρ, and composition y,

$$\begin{aligned} m_1 &= \rho_1^o V_1 = y\rho V, \\ m_2 &= \rho_2^o V_2 = (1-y)\rho V, \end{aligned}$$

where V_1 and V_2 are the volumes of the pure liquids, while V is the total volume of the mixture. Since for an ideal mixture the volume change of mixing $\Delta V_{mix} = 0$, we obtain,

$$V = V_1 + V_2 = \left(\frac{y\rho}{\rho_1^o} + \frac{(1-y)\rho}{\rho_2^o} \right) V.$$

This gives us the expression for ρ as a function of y,

$$\rho(y) = \frac{\rho_1^o \rho_2^o}{\rho_1^o - y(\rho_1^o - \rho_2^o)} = \frac{\rho_2^o}{1 - \epsilon y},$$

where $\epsilon = (\rho_1^o - \rho_2^o)/\rho_1^o$. If $\epsilon \ll 1$, then $\rho = \bar{\rho}\,(1 + \epsilon y)$.

In general, for a liquid mixture with a small density variation, the density $\rho(y)$ can be expanded about its average value, $\rho = \bar{\rho}(1 + \epsilon y)$, so that, to first-order accuracy in ϵ, the Navier-Stokes equation (2.28), the conservation of matter equation (2.16), and the equation of state (2.30) become, respectively,

$$\bar{\rho}\left(\frac{\partial \mathbf{v}}{\partial t} + (\mathbf{v}\cdot\nabla)\mathbf{v}\right) = -\nabla p + \nabla\cdot\left\{\eta\left[(\nabla\mathbf{v}) + (\nabla\mathbf{v})^{\dagger}\right]\right\} + \mathbf{F}_o + \bar{\rho}\mathbf{g} + \epsilon\mathbf{q}. \tag{2.31}$$

$$\frac{\partial y}{\partial t} + \mathbf{v}\nabla y = -\nabla\cdot\left(\frac{\mathbf{j}}{\bar{\rho}}\right) + \epsilon y\nabla\cdot\left(\frac{\mathbf{j}}{\bar{\rho}}\right). \tag{2.32}$$

$$\nabla\cdot\mathbf{v} = \epsilon\,\nabla\cdot\left(\frac{\mathbf{j}}{\bar{\rho}}\right). \tag{2.33}$$

where

$$\mathbf{q} = -y\left(-\nabla p + \nabla\cdot\left\{\eta\left[(\nabla\mathbf{v}) + (\nabla\mathbf{v})^{\dagger}\right]\right\} + \mathbf{F}_o + \bar{\rho}\mathbf{g}\right) + \nabla\left\{\left(\zeta - \frac{2}{3}\eta\right)\nabla\cdot\left(\frac{\mathbf{j}}{\bar{\rho}}\right)\right\}$$

2.6 Simplifying Assumptions

Now we restrict our problem to the early and medium-late stages of phase separation, when the characteristic size of the phase domains R are comparable with the characteristic period of initial instability $\lambda = 2\pi a(\Psi - 2)^{-1/2}$ [14]. For example, for values of the Margules parameter $\Psi = 2.1 - 3.0$, we do not expect R to exceed $100\,a$. Then, we can introduce the following simplifying assumptions.

A. Buoyancy forces are negligible. Capillary forces are much stronger than buoyancy forces, so that the size of the phase domains R is small enough to insure that $(R^2 g\Delta\rho/\sigma) \ll 1$.

B. *Inertial terms are negligible.* For small Reynolds numbers $Re = \rho v r/\eta \ll 1$. the inertial terms in the Navier-Stokes equation can be neglected.

C. *Density differences are small.* The densities of the two phases are very close to each other. so that $\rho \approx \bar{\rho} = const.$ and the $O(\epsilon)$-terms vanish from Equations (2.31) — (2.32). Then. the equation of state (2.33) reduces to the usual incompressibility constraint. $\nabla \cdot \mathbf{v} = 0$.

D. *Viscosity is uniform.* The two species A and B are assumed to have the same viscosity. When this assumption is violated. generalization is straightforward.

E. *Molecular weight is uniform.* Finally. we assume that the species A and B have the same molecular weights. i.e $M_A = M_B = M_W$. As the mole fraction is equal to the mass fraction. $y = x \equiv \phi$. both the diffusion flux (2.24) and capillary force (2.26) become functions of the dimensionless chemical potential $\tilde{\mu} = \mu_A - \mu_B$, i.e..

$$\frac{\mathbf{j}}{\rho} = -D\phi(1-\phi)\nabla\tilde{\mu} \qquad \mathbf{F}_\phi = \frac{\rho RT}{M_W}\tilde{\mu}\nabla\phi. \tag{2.34}$$

We also assume that. as the species A and B have physical properties that are close to each other. they have equal Margules parameters. $\Psi_A = \Psi_B = \Psi$. which simplifies the expression for the chemical potential (2.8).

$$\tilde{\mu} = \mu_0 + \log\frac{\phi}{1-\phi} + \Psi(1-2\phi) - a^2\nabla^2\phi. \tag{2.35}$$

After these assumptions, the set of equations (2.31-2.33) becomes,

$$\eta\nabla^2\mathbf{v} = \nabla p - \mathbf{F}_\phi. \tag{2.36}$$

$$\frac{\partial\phi}{\partial t} + \mathbf{v}\nabla\phi = -\nabla\cdot\left(\frac{\mathbf{j}}{\bar{\rho}}\right). \tag{2.37}$$

$$\nabla\cdot\mathbf{v} = 0. \tag{2.38}$$

where body force $\mathbf{F}_\phi$ and diffusive flux $\mathbf{j}$ are given by (2.34).

Now, we restrict our analysis to two-dimensional systems, so that the velocity $\mathbf{v}$ can be expressed in terms of a stream function ψ, i.e. $v_1 = \partial\psi/\partial r_2$ and $v_2 = -\partial\psi/\partial r_1$. Consequently, substituting (2.34) into (2.36-2.37), we obtain,

$$\frac{\partial\phi}{\partial t} = \nabla\psi\times\nabla\phi + D\nabla\cdot(\phi(1-\phi)\nabla\tilde{\mu}). \tag{2.39}$$

$$\eta\nabla^4\psi = \frac{\rho RT}{M_W}\nabla\tilde{\mu}\times\nabla\phi. \tag{2.40}$$

where

$$\mathbf{A}\times\mathbf{B} = A_1B_2 - A_2B_1.$$

Finally, substituting the expression (2.35) for the chemical potential into the system of equations (2.39) and (2.40), we obtain,

$$\frac{\partial\phi}{\partial t} = \nabla\psi\times\nabla\phi + D\,\nabla\cdot\left(\nabla\phi - \phi(1-\phi)\left[2\Psi + a^2\nabla^2\right]\nabla\phi\right). \tag{2.41}$$

$$\nabla^4\psi = -a^2\frac{\rho}{\eta}\frac{RT}{M_W}\nabla(\nabla^2\phi)\times\nabla\phi. \tag{2.42}$$

When viscosity is a known function of composition, $\eta = \eta(\phi)$, with $\eta' = d\eta/d\phi$ and $\eta'' = d^2\eta/d\phi^2$, the first member in (2.42) is replaced as follows,

$$\eta\nabla^4\psi \to \eta\nabla^4\psi + 2\frac{\eta'}{\eta}(\nabla\phi)\cdot(\nabla\nabla^2\psi) + \left[\frac{\eta'}{\eta}\nabla\nabla\phi + \frac{\eta''}{\eta}(\nabla\phi)(\nabla\phi)\right]\cdot\cdot\left[2\nabla\nabla\psi - \mathbf{I}\nabla^2\psi\right].$$

CHAPTER 3

GENERAL PROCEDURES

3.1 The Scaling

Since the main mechanism of mass transport at the beginning of the separation process is diffusion, the lengthscale of the process is the microscopic length a. Therefore, using the scaling:

$$\tilde{r} = \frac{1}{a} r, \qquad \tilde{t} = \frac{D}{a^2} t, \qquad \tilde{\psi} = \frac{1}{\alpha D} \psi, \tag{3.1}$$

we obtain,

$$\frac{\partial \phi}{\partial \tilde{t}} = \alpha \tilde{\nabla} \tilde{\psi} \times \tilde{\nabla} \phi + \tilde{\nabla} \cdot \left(\tilde{\nabla} \phi - \phi (1 - \phi) \left[2\Psi + \tilde{\nabla}^2 \right] \tilde{\nabla} \phi \right), \tag{3.2}$$

$$\tilde{\nabla}^4 \tilde{\psi} = -\tilde{\nabla} (\tilde{\nabla}^2 \phi) \times \tilde{\nabla} \phi \tag{3.3}$$

where

$$\alpha = \frac{a^2}{D} \frac{\rho}{\eta} \frac{RT}{M_W} \tag{3.4}$$

The non-dimensional number α is the ratio between convective and diffusive mass fluxes in the convection-diffusion equation (3.2) and can be interpreted as the Peclet number, i.e. $\alpha = Va/D$. Here, V is a characteristic velocity, which can be estimated through (2.36) and (2.34) as $V \sim F_o a^2/\eta$, where $F_o \sim \rho RT/(aM_W)$.

At the later stages of phase separation, when the system is composed of patches of almost constant compositions ϕ and $\phi+\Delta\phi$, separated by sharp interfaces, the parameter α can also be interpreted as the inverse of the capillary number [22], $Ca = \eta U/\sigma$, with $U = \sqrt{\Psi-2}\,(\Delta\phi)_{eq}^2\, D/a$ denoting a characteristic diffusion velocity. In fact, considering that, the characteristic length a is proportional to the surface tension at equilibrium σ [5], we obtain,

$$\sigma = \frac{1}{2}\frac{\rho RT}{M_W}a^2\int(\nabla\phi)^2dx \sim \alpha D\eta\,\frac{(\Delta\phi)_{eq}^2}{\ell^2}\,\ell \sim \alpha\frac{D\eta}{a}(\Psi-2)^{3/2}. \tag{3.5}$$

where $(\Delta\phi)_{eq} \sim \sqrt{\Psi-2}$ is the composition difference between the two phases at equilibrium and $\ell \sim a/\sqrt{\Psi-2}$ is the width of interface [14], so that $Ca = \alpha^{-1}$. Note, that the expression (3.5) allows us to estimate physical value for the microscopic length a,

$$a \sim (\Psi-2)^{-3/2}\,\frac{\sigma\, M_W}{\rho RT}. \tag{3.6}$$

A parameter similar to α, called "fluidity" parameter, was also defined by Tanaka and Araki [19]. For systems with very large viscosity, α is small, so that the model describes the diffusion-driven separation process of polymer melts and alloys [14]. For most liquids, however, α is very large, with typical values ranging from 10^3 to 10^5. Therefore, it appears that diffusion is important only at the very beginning of the separation process, in that it creates a non-uniform concentration field. Then, the concentration-gradient-dependent capillary force induces the convective material flux which is the dominant mechanism for mass transport. At no time, however, the

diffusive term in Eq. (3.3) can be neglected, as it stabilizes the interface and saturates the initial exponential growth. In addition, it should be stressed that the stream function ψ depends on high order derivatives of the concentration and therefore it is very sensitive to the concentration profile within the interface.

3.2 Numerical Procedure

In the following, we present the numerical solutions of equations (3.2)-(3.3) corresponding to temperature quenches where the Margules parameter Ψ increases from $\Psi_i = 2$ (which is its critical value) to some value Ψ_w, in the range from $\Psi_w = 2.1$ to $\Psi_w = 3$. In most cases, we consider instant quenches, where systems with uniform concentration field ϕ_0 experience an instant drop of Margules parameter from Ψ_i to Ψ_w. We consider both critical ($\phi_0 = 0.5$) and off-critical ($\phi_0 < 0.5$) quench.

Equations (3.2)-(3.3) were solved using an explicit finite difference method on a uniform two–dimensional grid $[(i\triangle x, j\triangle y), i = 1..N, j = 1..N]$ with spacing varying from $\triangle x/a, \triangle y/a = 0.5$ for $\Psi = 3$ to $\triangle x/a, \triangle y/a = 2$ for $\Psi = 2.1$. We adopted a cell-centered representation for the concentration variable $\phi^n_{ij}(t)$, and discretized the right-hand sides of Eq. (3.2)-(3.3) in flux conservation form, using a fourth-order accurate approximation of the spatial derivatives. Equation (3.2) was advanced in time, using a straightforward explicit Eulerian step, and we chose the time step $\triangle t$ in such a way to satisfy the CFL stability condition, so that the numerical scheme was $O(\triangle x^4, \triangle t)$ accurate. The biharmonic equation (3.3) was solved using standard

DBIHAR package [34]. Boundary conditions were no-flux (or periodic in some special cases) for the concentration field and no-slip for the velocity field.

The background noise was simulated generating a random concentration field of amplitude, which was uncorrelated both in space and in time. That means that at each time step a spatially uncorrelated noise was added to the concentration field, and was then subtracted at the next time step, only to be replaced with another spatially uncorrelated background noise of the same amplitude. To estimate the amplitude of the noise let us consider the contribution to the material flux due to thermal fluctuations, which satisfies the fluctuation-dissipation theorem [31].

$$\begin{aligned} \langle \delta \mathbf{j}(\mathbf{r}, t) \rangle &= 0, \\ \langle \delta \mathbf{j}(\mathbf{r}, t)\ \delta \mathbf{j}(\mathbf{r}', t') \rangle &= -\frac{2}{n} D\, \mathbf{I}\, \phi(1-\phi)\delta(\mathbf{r}-\mathbf{r}')\delta(t-t'), \end{aligned}$$

with the brackets indicating ensemble averages, and n denoting the number density, that is the number of particles per unit volume. Trivially, if we also assume that the temperature quench is instantaneous, so that the temperature is uniform within the system and Ψ is constant, this equation reduces to the one considered in [14]. In dimensionless variables (3.1) the noise above becomes,

$$\begin{aligned} \left\langle \delta \tilde{\mathbf{j}}(\tilde{\mathbf{r}}, \tilde{t}) \right\rangle &= 0, \\ \left\langle \delta \tilde{\mathbf{j}}(\tilde{\mathbf{r}}, \tilde{t})\ \delta \tilde{\mathbf{j}}(\tilde{\mathbf{r}}', \tilde{t}') \right\rangle &= -2\, \mathbf{I}\, \varepsilon^2 \phi(1-\phi)\delta(\tilde{\mathbf{r}}-\tilde{\mathbf{r}}')\delta(\tilde{t}-\tilde{t}'). \end{aligned}$$

with $\varepsilon = (na^3)^{-1/2}$. In our simulation we used a noise with amplitude

$$\delta\phi = \frac{\varepsilon}{(\triangle x/a)(\triangle tD/a^2)} \approx 0.001 - 0.1. \tag{3.7}$$

3.3 Interpretation of Results

3.3.1 Domain Size

The most important characteristic of phase separating system is the growth rate of domains formed by different phases, and the most natural choice for a length-scale is the equivalent radius.

$$R = \sqrt{\langle A \rangle / \pi} \tag{3.8}$$

where A is the area of a single-phase domain. Nevertheless, this approach is not suitable for systems forming long interconnected domains instead of isolated drops. In these systems, the domain width R_F is a characteristic lengthscale, which can be found using the following expression.

$$R_F = \frac{\sum (\phi_k / k)}{\sum \phi_k}. \tag{3.9}$$

where ϕ_k is the Fourier transform of the concentration distribution field $\phi(r)$, defined in $\phi = \sum \phi_k e^{ikr}$. Another way to estimate the typical size of phase domains was introduced by Desai *et al.* [35], who considered the radial pair correlation function.

$$C(r) = \sqrt{\frac{1}{2\pi} \int_0^{2\pi} \langle \phi(\mathbf{r}' + \mathbf{r}) \phi(\mathbf{r}') - \phi_0^2 \rangle \, d\theta}; \qquad \mathbf{r} = (\mathbf{r}, \theta). \tag{3.10}$$

and defined the typical size R_D as its first zero.

$$C(R_D) = 0. \tag{3.11}$$

It should be mentioned that the correlation function itself has interesting features, for example self-similarity in case of diffusion-driven system (see Section 4.4).

3.3.2 Domain Composition

Another interesting property characterizing the decomposing system is the average composition inside the domains, although it is often neglected as a result of the local equilibrium assumption. To describe the average composition inside the domains, we define the separation depth s, measuring the "distance" of the single-phase domains from their equilibrium state, i.e.,

$$s = \left\langle \frac{\phi(\mathbf{r}) - \phi_0}{\phi_{eq}(\mathbf{r}) - \phi_0} \right\rangle. \tag{3.12}$$

where ϕ_0 is the initial composition, and the bracket indicates volume average. Here ϕ_{eq} is the steady state composition of the A-rich phase, ϕ_{eq}^A, or the B-rich phase, ϕ_{eq}^B, depending on the local composition $\phi(\mathbf{r})$.

$$\begin{aligned} \phi_{eq}(\mathbf{r}) &= \phi_{eq}^A, \qquad \phi(\mathbf{r}) > \phi_0, \\ \phi_{eq}(\mathbf{r}) &= \phi_{eq}^B, \qquad \phi(\mathbf{r}) < \phi_0. \end{aligned}$$

Defined in this way, the separation depth s is zero for perfectly mixed system, then monotonically increases during the separation process, an finally it approaches unity

Ψ	ϕ_{eq}^{A}	ϕ_{eq}^{b}
2.1	0.6853	0.3147
2.2	0.7515	0.2485
2.3	0.7961	0.2039
2.4	0.8293	0.1707
2.5	0.8552	0.1448
2.7	0.8931	0.1069
3.0	0.9293	0.0707

Table 1. Equilibrium compositions of phases ϕ_{eq}^{A} and ϕ_{eq}^{B} for different values of Margules parameter Ψ

asymptotically for $t \to \infty$. The equilibrium compositions ϕ_{eq}^{A} and ϕ_{eq}^{B} are the functions of the Margules parameter Ψ only. and can be found from the mean field self-consistency equation as [31],

$$\left(\phi_{eq}^{A,B} - \frac{1}{2}\right) = \frac{1}{2}\tanh\left[\Psi\left(\phi_{eq}^{A,B} - \frac{1}{2}\right)\right].$$

The values of Ψ used in our simulations. together with the corresponding equilibrium compositions ϕ_{eq}^{A} and ϕ_{eq}^{B}, are given in Table 1.

CHAPTER 4

DIFFUSION DRIVEN PHASE SEPARATION

Let us consider a system with very large viscosity, as in binary alloys and polymer mixtures, so that the diffusion flux in Equation (3.2) is much larger than the convective flux, i.e. $\alpha = 0$. In this case, the system (3.2)-(3.3) reduces to a single equation.

$$\frac{\partial \phi}{\partial \tilde{t}} = \tilde{\nabla} \cdot \left(\tilde{\nabla} \phi - \phi(1-\phi) \left[2\Psi + \tilde{\nabla}^2 \right] \tilde{\nabla} \phi \right). \tag{4.1}$$

The one-dimensional version of this equation was solved by Mauri *et al.* [14] for periodic and pulsed initial conditions, using split-step method in time and pseudo spectral collocation method in space.

4.1 One-dimensional Systems

First, we validated our numerical scheme by solving the one-dimensional version of equation (4.1) with periodic boundary conditions, considering an instantaneous, critical and uniform quench with $\Psi = 3$ and $\phi_0 = 0.5$. As we mentioned above, in this case our equation and boundary conditions become essentially the same as those used in [14], the only difference being that the initial conditions and the numerical technique employed here are different. As we can see in Fig.1, identical results were obtained, as initial, exponentially growing instabilities are later saturated by the

effect of the non-linear terms. Eventually, the concentration distribution tends to a steady state, periodic profile, with a period and an amplitude which correspond to the fastest growing mode of the linear regime [14].

$$\lambda = \frac{2\pi a}{\sqrt{\Psi - 2}}. \tag{4.2}$$

Qualitatively, the relaxation time that is needed to reach steady state also agrees with that obtained in [14], i.e. λ^2/D.

Our next step was to study a critical quench where temperature, and therefore Ψ, is a known function of position and time. Since near the critical point we have $\Psi \propto (T - T_{cr})$, then $\Psi(x,t)$, with $0 \leq x \leq L$, can be obtained from the heat conduction equation, $\partial\Psi/\partial t = k\ \partial^2\Psi/\partial x^2$, with initial and boundary conditions, $\Psi(x,0) = \Psi_i$ and $\Psi(0,t) = \Psi(L,t) = \Psi_w$, describing the heat propagation from the walls of the container towards the center. Typical solutions for $\phi(x,t)$, together with the corresponding $\Psi(x,t)$, are given in Figure 2, where no-flux boundary conditions have been applied. From the sequence of plots in Figure 2 it is easy to see that the instability propagates from the edges towards the center of the cell, growing without changing its lengthscale until the equilibrium state is reached. As shown in Figure 3, the steady state concentration distribution appears to be periodic across the domain, provided, naturally, that the cell size L is either much larger than, or an exact multiple of, the droplet size; if none of these conditions is satisfied, the periodic steady state solution can never be reached, as it is evident from the concentration profile

at the bottom of Figure 3. The period of the steady state solutions decreases as the thermal diffusivity k increases, until, when $k > D$, it becomes equal to the period λ obtained for instant quenching, with $k \to \infty$. Clearly, since in most cases we have $k \gg D$, this result shows that the assumption of instant quenching is very reasonable. Our results can be considered an extension of those obtained by Carmesin *et al.* [36], who studied the influence of a continuous quenching on the initial stages of spinodal decomposition by using the linearized theory of spinodal decomposition.

4.2 Two-dimensional Systems

First, equation (3.2) was solved for an instantaneous, critical quench, with periodic boundary conditions. Our simulations showed that at first the system tends to form circular drops whose size, λ, equals that of the one dimensional domains. However, unlike the one-dimensional case, this is not the steady state solution (see Figure 4), as the system rapidly evolves towards the formation of single-phase microdomains separated by sharp interfaces, which then merge to form filaments. This bicontinuous infinite-cluster morphology has been observed experimentally in binary fluid mixtures by Cumming *et al.* [37], and has been numerically simulated, among others, by Rogers, Elder and Desai [35] and by Farrell and Valls [18]. Our simulations show that this dendroid-like structure continues to deform, increasing its thickness, and, above all, further reducing the total area of the interface. So, for example, microdomains of one phase entirely surrounded by the other phase evolve towards

assuming a spherical shape. However, contrary to the behavior of mixtures of totally immiscible liquids, these small, isolated drops continue to deflate even after they become spherical, until they diffuse out completely (see the evolution of the drop located in the lower left part of Figure 4).

As expected, a different morphology is obtained for non-isotropic systems. For example, in Figure 5 we show the concentration distribution in a system with periodic boundary conditions in the horizontal direction, and no-flux boundary conditions at the walls in the vertical direction, thereby simulating the behavior of a long horizontal tube. As the walls of the tube are quenched, the temperature of the whole system changes in time towards its steady state. As expected, the morphology of the system is composed of 'serpentines' with a well specified horizontal preferential direction, forming typical striped pattern as in Sagui and Desai [38]. As in the one-dimensional case, the thickness of these stripes increases as the heat conductivity of the system decreases.

4.3 Evolution of the Domain Composition

In Figure 6 the separation depth s, defined in Eq. (3.12) is plotted as a function of time, showing that the phase separation process can be divided into three stages. During the first stage, $t < t_0$, the concentration ϕ remains approximately constant, i.e. there is no phase separation; then, for $t_0 < t < t_1$, the concentration changes rapidly, with the exact values of t_0 and t_1 defined such that this rate of

change is larger than a given critical value: finally, during the third stage, $t > t_1$, the separation depth s increases much more slowly. As shown in Figure 7, the value of t_0 depends on the depth of the temperature quench, $(\Psi - 2)$, and the amount of the random noise, $\delta\phi$, through the correlation $t_0 = (A - B \log \delta\phi) / (\Psi - 2)^c$, where A, B and c are constant that depend on the value of ϕ_0. As for the second stage, the time interval $(t_1 - t_0)$ appears to be independent of the random noise (see Figure 7), and is approximately equal to the relaxation time λ^2/D. Finally, during the last stage, $t > t_1$, the separation depth s continues to change, although more gradually, tending asymptotically to 1, indicating that, although the system is composed of single-phase domains separated by sharp interfaces, the composition inside these domains is not equal to its final equilibrium value. Therefore, the local equilibrium assumption stating that no change in composition occurs after the formation of sharp interfaces, is not valid, and therefore most of the scaling concepts should be revised. Although an identical conclusion was reached by Tanaka and Araki [19] in the case of fluid systems, this is the first time that a strong violation of local equilibrium is observed for spinodal decomposition under small, or zero, fluidity conditions.

4.4 Temporal Growth of the Domain Size

During the last stage of the separation process, the characteristic size of the microdomains appears to be independent of the depth of the temperature quench and of the background noise and, as shown in Figure 8, it grows according to the 1/3

law predicted by Lifshitz and Slyozov [39]. In Figure 8 we plotted the characteristic length, R_F, defined in Equation(3.9), showing that $R(t) \propto (aDt)^{1/3}$. These results are in agreement with those of Desai *et al.* [35], who defined the typical size R_D as the first zero of the radial pair correlation function (3.11). In Figure 9, $C(r,t)$ is plotted as a function of r for different t, showing that the different curves collapse into a self-similar solution, $g(z)$, with $z = r(aDt)^{-1/3}$.

4.5 Off-critical Quenches

We have also studied the phase separation due to an off-critical quench, in which $\phi_0 = 0.4$, i.e. in which there is more A than B. As expected, instead of interconnected domains, we observe the formation of isolated drops of the B-rich phase immersed in one large domain of the A-rich phase (see Fig. 10), in agreement with some previous theoretical [18, 40, 35] and experimental [37] findings, and consistent with the experimental evidence [23] that stable emulsions tend to form when a liquid mixture is quenched within the meta-stable region of its phase diagram.

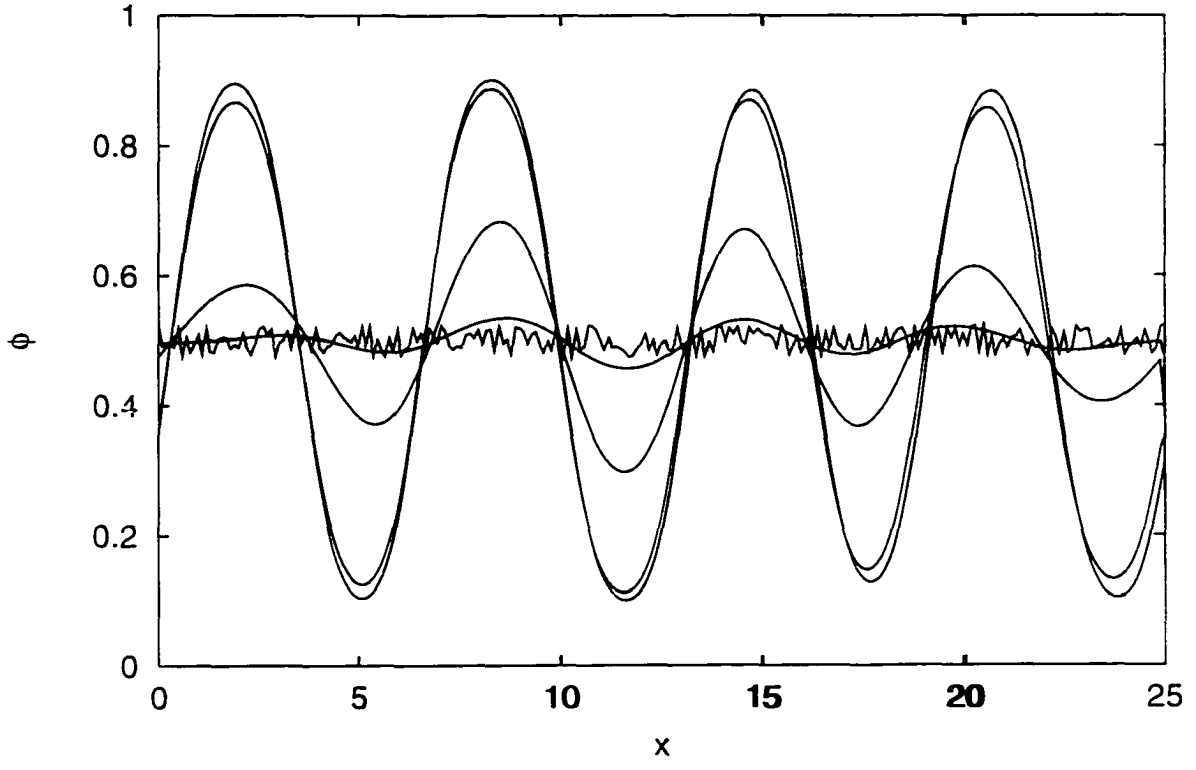

Figure 1. Composition as a function of position for a critical instantaneous quench $\Psi = 3$ at different times, when a random perturbation with amplitude $\delta\phi = 0.025$ is superimposed to the initial composition $\phi = 0.5$. The space and time coordinates, x and t, are scaled in terms of a and a^2/D, respectively. The curves correspond respectively to times $t = 0$, 0.5, 1.0, 1.5 and 2.5.

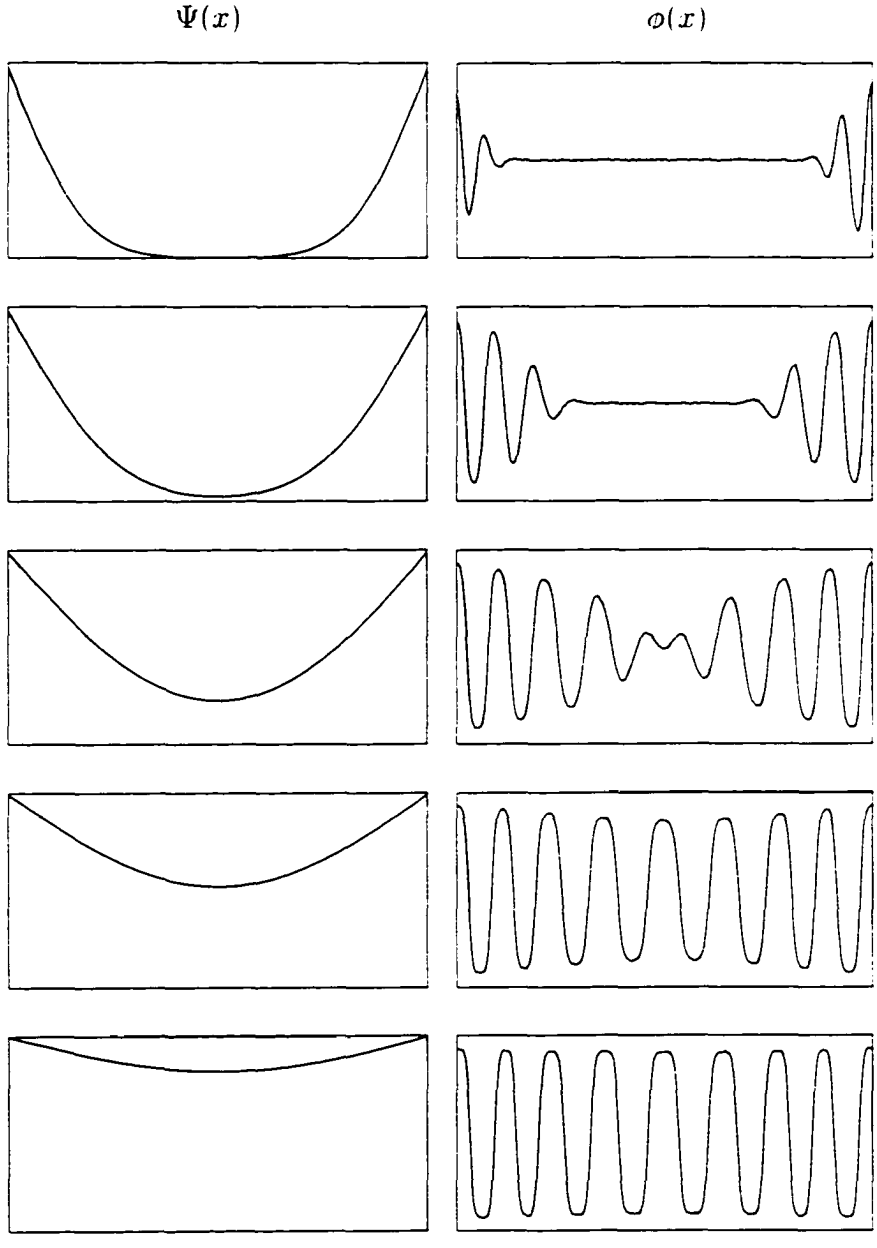

Figure 2. Quenching depth, Ψ, and composition, ϕ, as functions of position at different times for heat diffusivity $\alpha = D$. The curves correspond to times $t = 100, 200, 500, 1000$ and 2000 (given in a^2/D-units). The spatial coordinate varies between 0 and $100\,a$, composition varies between 0 and 1, while the quenching depth solves the heat equation with $\Psi_i = 2$ and $\Psi_w = 3$.

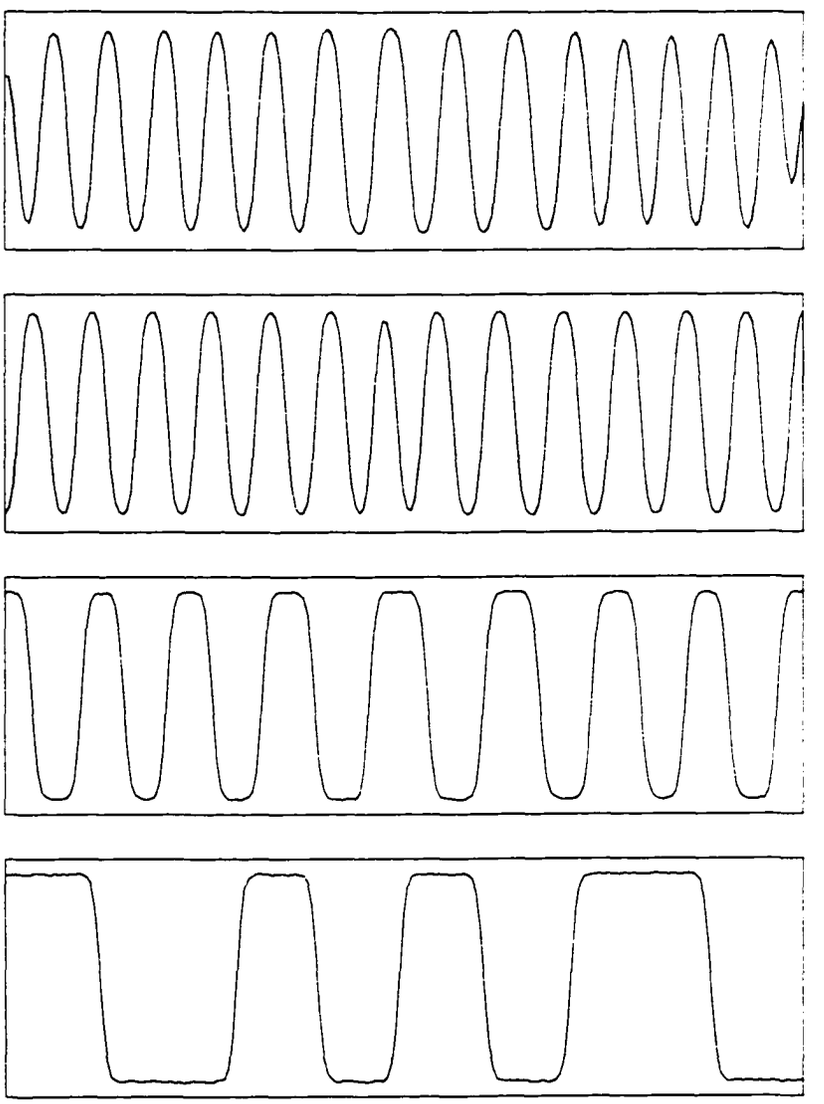

Figure 3. Steady state composition as function of position for different values of the heat diffusivity. $k = \infty$ (i.e. instant quenching). $10\,D$. $1\,D$ and $0.1\,D$. respectively. The spatial coordinate varies between 0 and $100\,a$. while composition varies between 0 and 1.

Instantaneous quench of mixture with average composition $\phi = 0.5$.

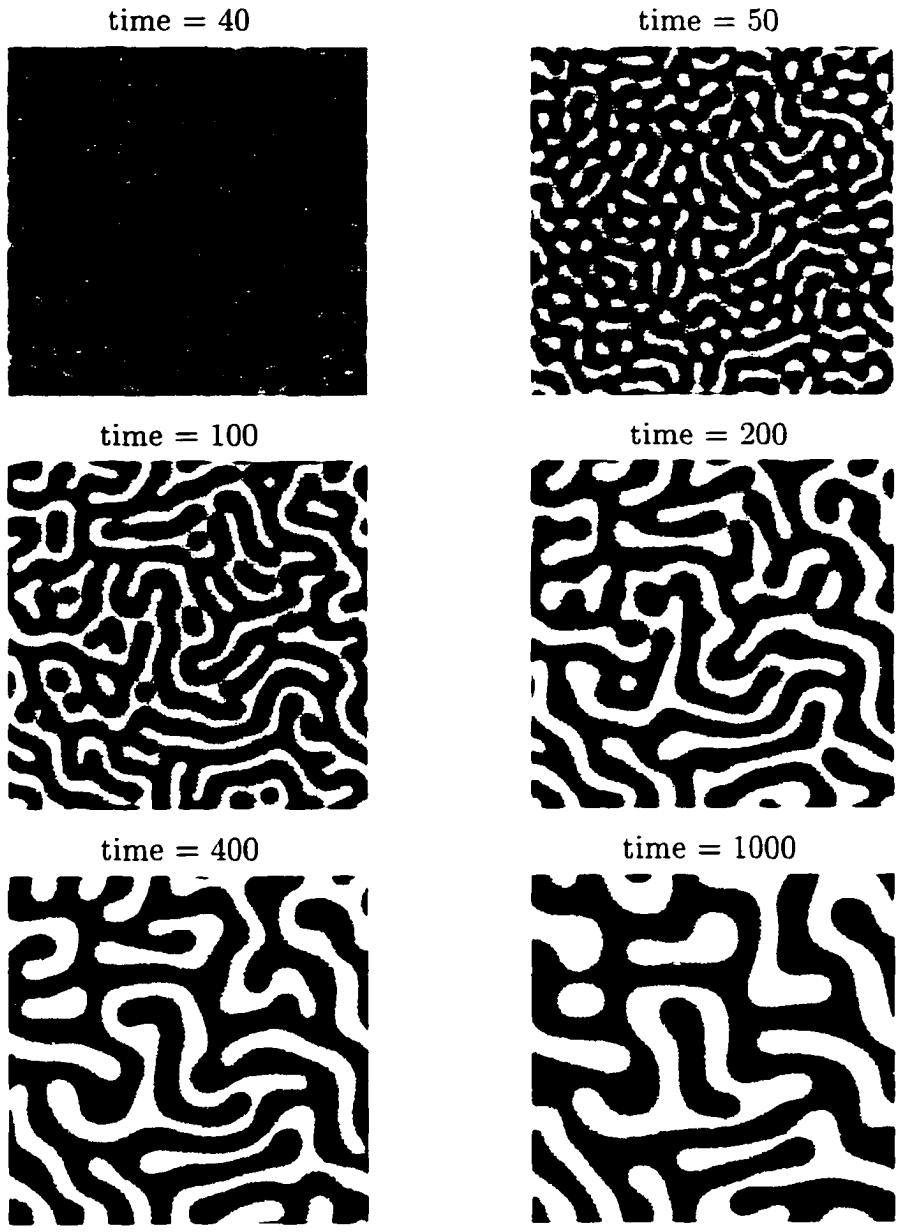

Figure 4. Composition as a function of position for a critical instantaneous quench $\Psi = 3$ at different times. The size of the system is $100a \times 100a$. with periodic boundary conditions. Snapshots correspond respectively to times $t = 20.\ 60.\ 100.\ 500.\ 1000$ and $2000.$ expressed in a^2/D-units. The gray level varies linearly between black and white. corresponding to a concentrations $\phi = \phi^A_{eq}$. and $\phi = \phi^B_{eq}$. respectively.

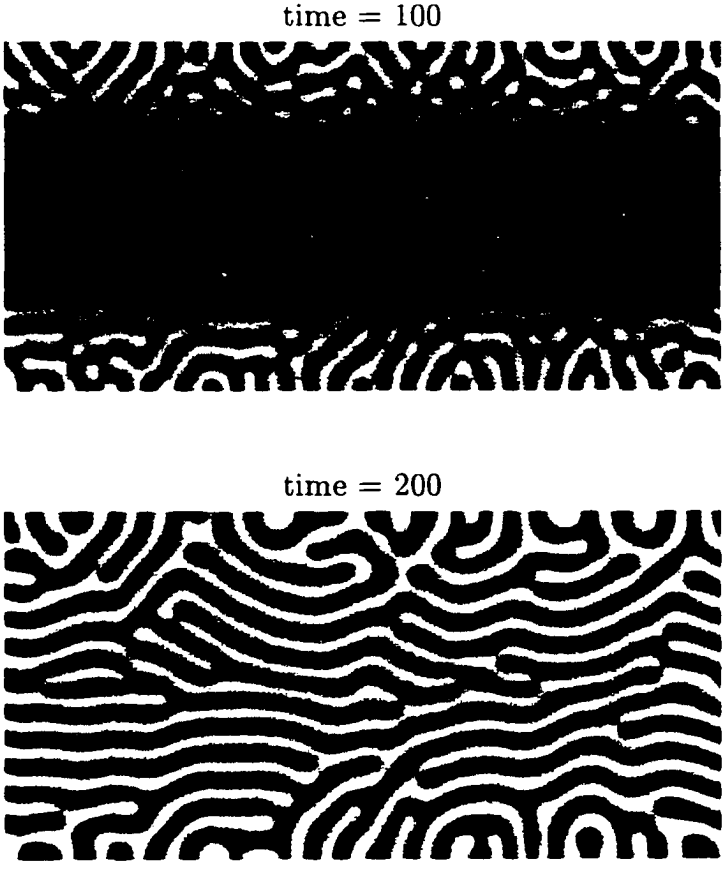

Figure 5. Composition as a function of position at different times after the temperature of the upper and lower walls has been quenched from $\Psi_i = 2$ to $\Psi_w = 3$, with heat diffusivity $k = 10D$. The size of the system is $200a \times 100a$, with periodic boundary conditions in the horizontal direction, and no-flux boundary conditions in the vertical direction, to simulate a long, horizontal tube. Snapshots correspond respectively to times $t = 100$, 200, and 400, expressed in a^2/D-units. The gray level varies linearly between black and white, corresponding to a concentrations $\phi = \phi^A_{eq}$, and $\phi = \phi^B_{eq}$, respectively.

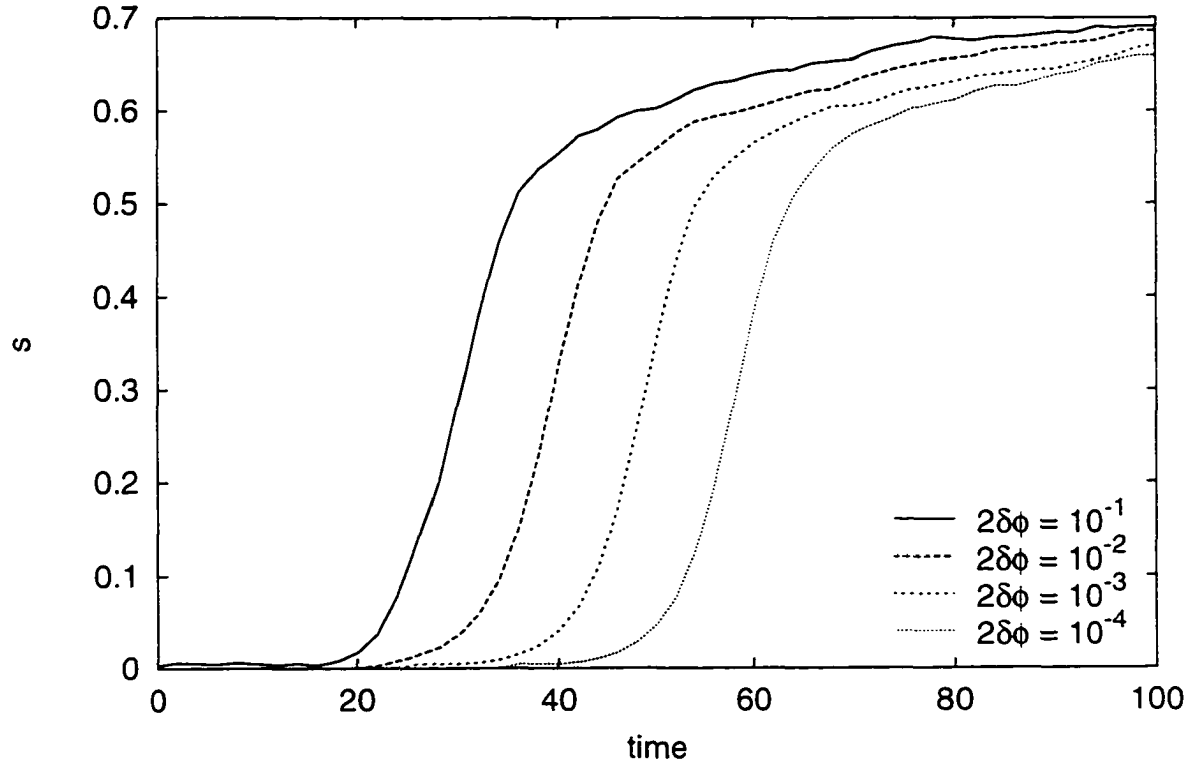

Figure 6. Separation depth, s, as a function of time for a critical instantaneous quench $\Psi = 3$ and different amplitudes of the background noise, $\delta\phi = 0.5 \times 10^{-1}$, 0.5×10^{-2}, 0.5×10^{-3} and 0.5×10^{-4}, with time expressed in terms of a^2/D.

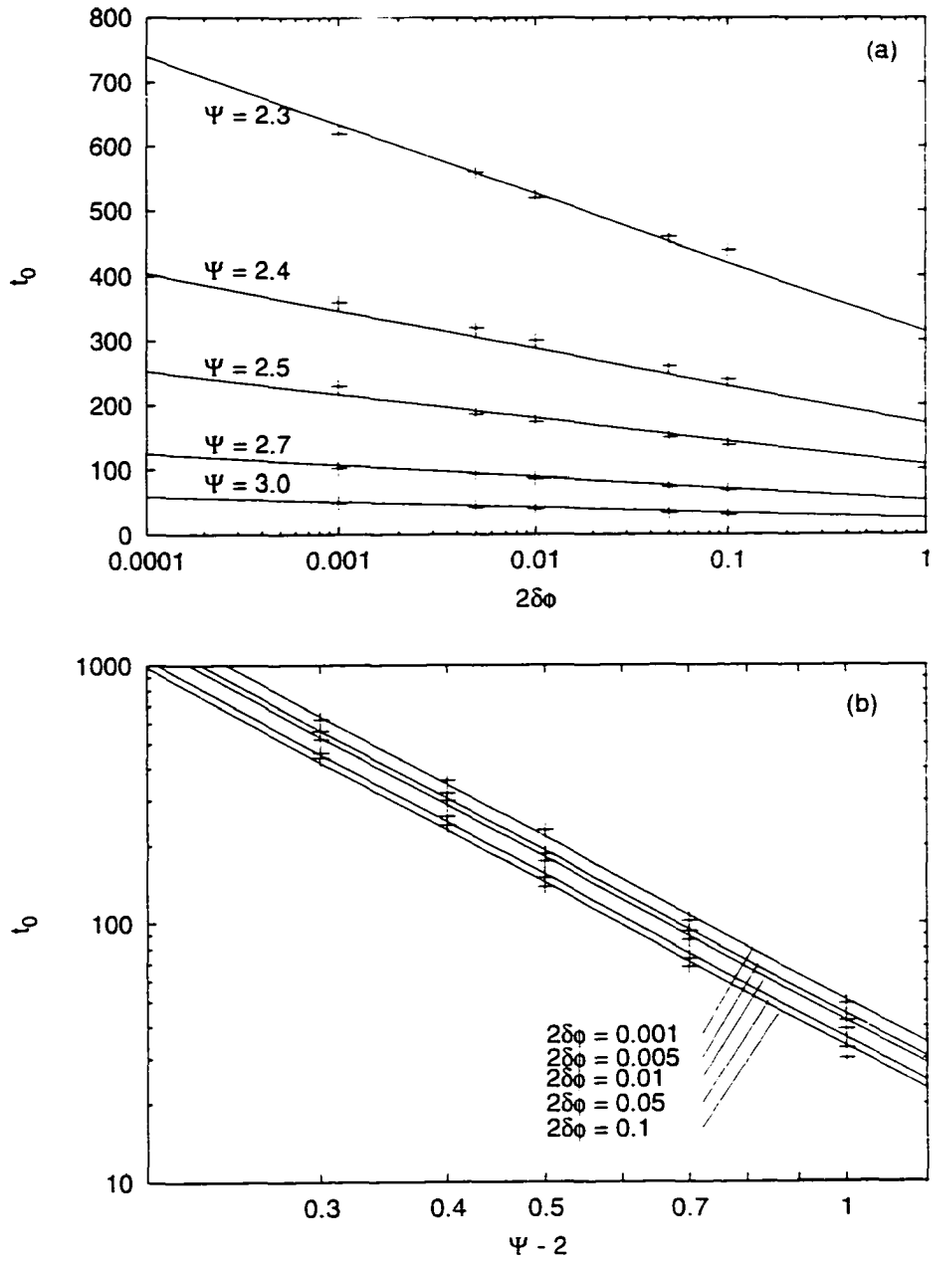

Figure 7. Initial time t_0 as a function of the background noise $\delta\phi$ (a) and the quenching depth $(\Psi - 2)$ (b). Points refer to the results of numerical simulations with $\phi_0 = 0.5$. while the continuous line represents the correlation $t_0 = (A - B \log \delta\phi) / (\Psi - 2)^c$. with $A = 22.5$. $B = 3.7$ and $c = 2.1$.

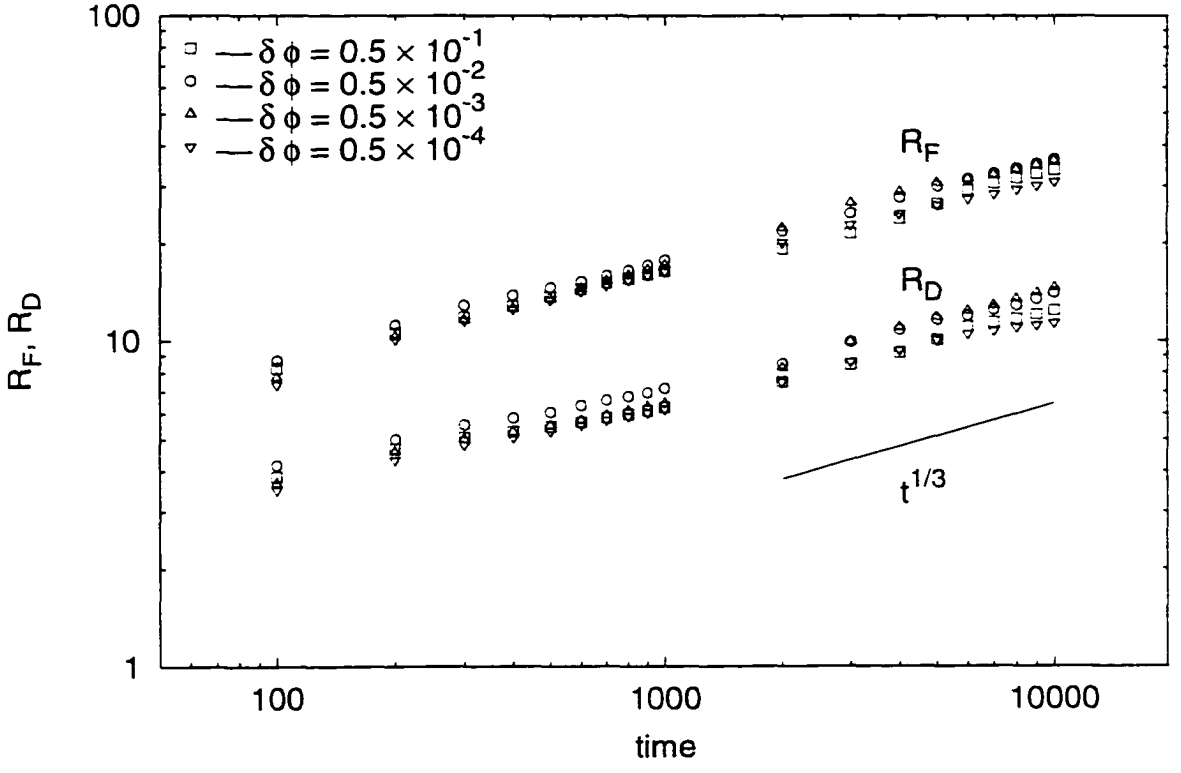

Figure 8. Characteristic size of the microdomains. R_F, expressed in a-units, as a function of time, t, expressed in a^2/D-units, after an instantaneous critical quench $\Psi = 3$. The lengthscale R_F is compared to R_D, representing the characteristic size of the microdomains as defined by Desai *et al.* [35]. The continuous line represents the correlation $R = 10\, t^{1/3}$

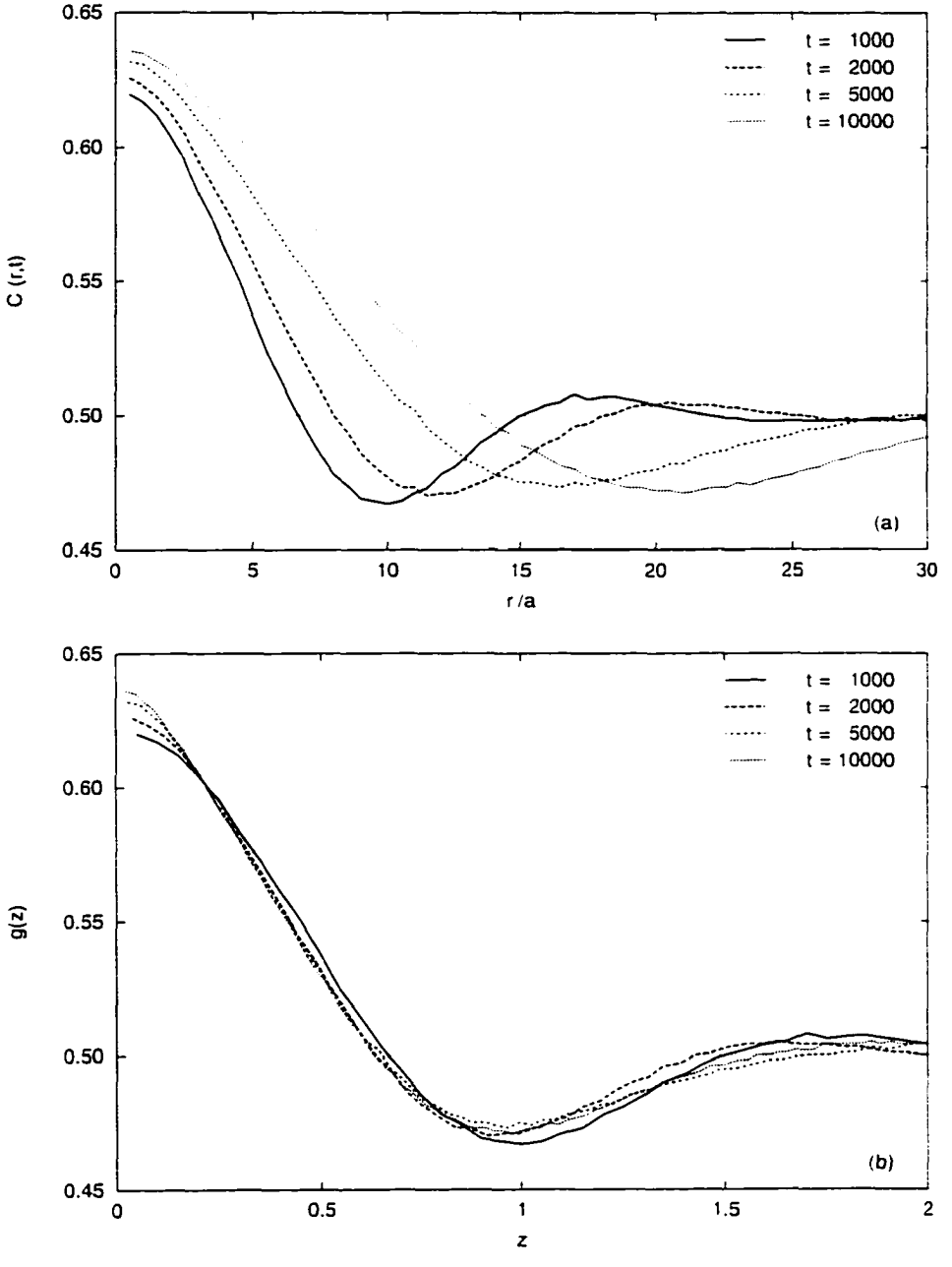

Figure 9. Radial pair correlation function, $C(r,t)$, after an instantaneous critical quench $\Psi = 3$, as a function of r for different t (a), and as a function of the self-similar parameter $z = r\,(aDt)^{-1/3}$ (b).

Instantaneous quenching of mixture with average composition $\phi = 0.4$.

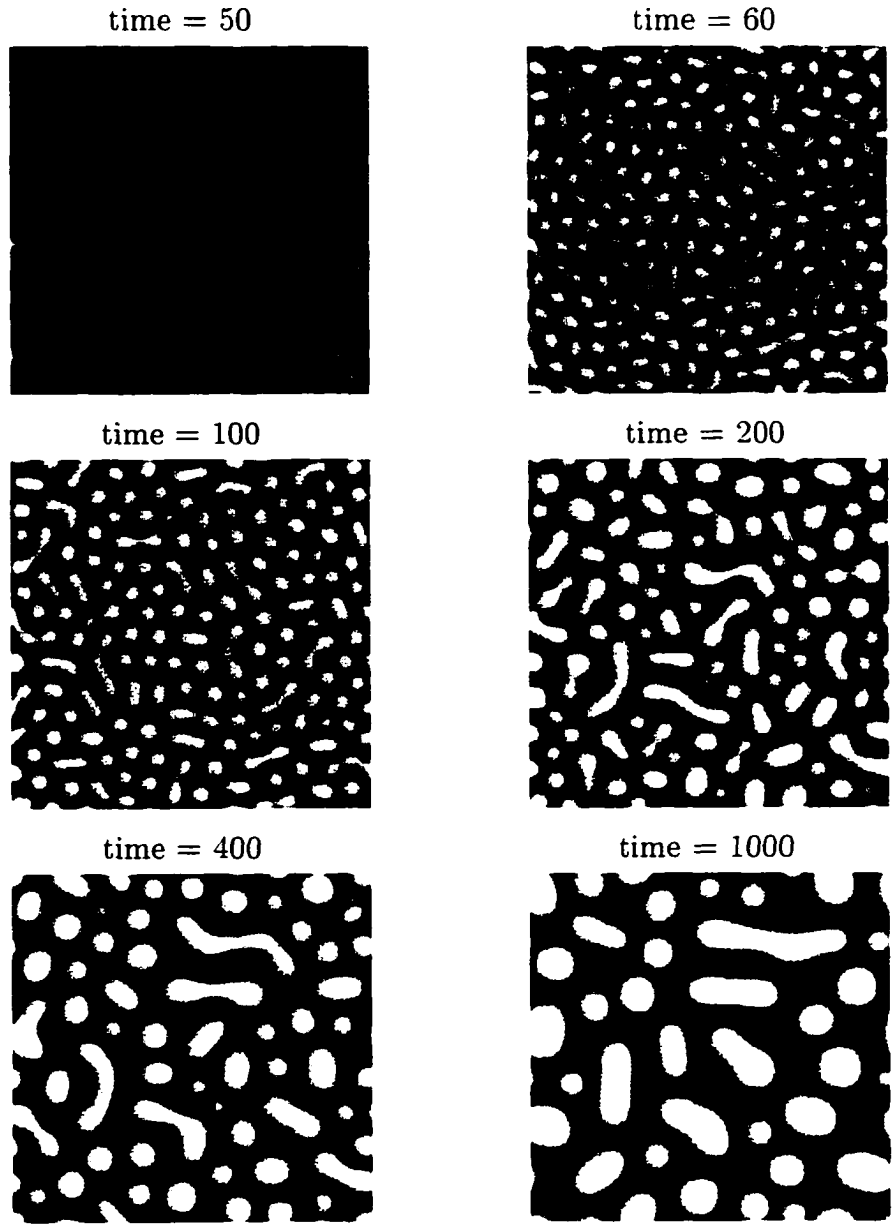

Figure 10. Composition as a function of position for $\Psi = 3$ at different times after an instantaneous off-critical quench with $\phi_0 = 0.4$. The size of the system is $100a \times 100a$, with periodic boundary conditions. Snapshots correspond to times $t = 20$, 60, 100, 500, 1000 and 2000, expressed in a^2/D-units. The gray level varies linearly between black and white, corresponding to a concentrations $\phi = \phi^A_{eq}$, and $\phi = \phi^B_{eq}$, respectively.

CHAPTER 5
CONVECTION DRIVEN PHASE SEPARATION

In this section, we describe the results of the numerical simulations of the model H described by Equations (3.2)-(3.3). The boundary conditions were no-flux for the concentration field and no-slip for the velocity field. In most of our simulations we used $\Psi = 2.1$, because this is the Margules parameter of the water-acetonitrile-toluene mixture with 20^oC temperature quench that was used in a parallel experimental study [23]. Both critical and off-critical quenches were considered, with uniform initial concentration fields $\phi_0 = 0.5$ and $\phi_0 = 0.4$, respectively. In this chapter, time is measured as $t = (10^5 a^2/D)\,\tau$, where τ is a non-dimensional time. Since typical values of D and a are $10^{-5} cm^2/s$ and $10^{-5} cm$, respectively, then $\tau \sim t/(1s)$.

5.1 Influence of Convection

First, we solved Eqs. (3.2)-(3.3) for a system with uniform initial mole fraction $\phi_0 = 0.5$ and for different values of the Peclet number α. The first row of images on Figure 11 represents the results for $\alpha = 0$, e.g. for the case when diffusion is the only mechanism of mass transfer, showing that, soon after the first drops appear, they coalesce into dendroid-like structures. The mean composition

within (and without) these structures changes rapidly, as at time $\tau = 0.05$ we already see two clearly distinguishable phases with almost uniform concentrations equal to 0.59 and 0.41, while at equilibrium their respective compositions are $\phi_{eq}^{A} = 0.685$ and $\phi_{eq}^{B} = 0.315$. After this early stage, the structures start to grow, increasing their thickness and reducing the total interface area, while at the same time the composition within the domains approaches its equilibrium value. This, however, is a slow process, driven only by diffusion, and at time $\tau = 0.1$ the phase domains still have a dendroid-like geometry with a characteristic width which is just twice as large as its initial value. In the following, we will denote these slow-changing configurations as metastable states, referring to Refs. [15, 35] for further informations on their evolution.

For non-zero convection, i.e. for $\alpha \neq 0$, dendritic structures thicken faster, but up to $\alpha \approx 10^2$ domain growth still follows the same pattern as for $\alpha = 0$: first, single-phase domains start to appear, separated from each other by sharp interfaces, and only later these structures start to grow, with increasing growth rate for larger α. When $\alpha > 10^2$, however, phase separation occurs simultaneously with the growth process. For example, when $\alpha = 10^4$, we see the formation of isolated drops of both phases, surrounded by the bulk of the fluid mixture, which is still not separated. In addition, drops appear to move fast and randomly while they grow, absorbing material from the bulk, colliding with each other and coalescing, so that single-phase domains grow much faster than when molecular diffusion is the only transport mechanism. In

fact, at time $\tau = 0.1$, single-phase domains have reached a size comparable to that of the container's (i.e. $400a$), while at that same time, in the absence of convection, the dendroid domains have an approximate widths of $20a$. Clearly, since the motion of the interface is too quick for the concentration diffusion to establish a metastable state within the microdomains, double, or multiple, phase separation is observed, in agreement with previous numerical [19, 22] and experimental [23, 41] results.

Although the dynamics of phase separation in fluids is mostly driven by convection, this is not the case for very short times. Then, the convective driving force $\mathbf{F}_\phi$ is negligible, as composition gradients did not develop yet, and therefore diffusion is the only mechanism of mass transport. In fact, the two pictures in Figure 12 show that at time $\tau = 0.02$ the concentration fields for $\alpha = 0$ and $\alpha = 10^4$ are almost indistinguishable from each other, with patterns having a characteristic period, λ, equal to the fastest growing mode in the linear regime for a diffusion-driven process [14].

5.2 Evolution of the Domain Composition

In Figure 13 the separation depth s for critical quenches is plotted as a function of time, showing the influence of the convection parameter α on the average phase composition within the phase domains. No detectable phase separation takes place when $\tau < 0.02$, that is until the first spinodal decomposition pattern is formed. Then, phase separation appears to take place in two different ways, depending on

whether $\alpha < 10^2$ or $\alpha > 10^3$. For smaller α's, we observe a fast separation process during the short time interval $0.02 < \tau < 0.06$, followed by slower growth of the separation depth. Comparing Figure 11 with Figure 13, we see that single-phase domains are formed during this fast separation process, and at time $\tau \sim 0.06$, they already appear to be separated by sharp interfaces. From that point on, separation proceeds much more slowly, as the concentration gradients within the single-phase domains are very small, while the concentrations of the two phases across any interface change only slowly in time. Although Tanaka [41] denotes these states as ones of local equilibrium, here we prefer to use the term "metastable states", considering that at stable equilibrium we must have $s = 1$, while here we have $s \leq 0.8$. In the case of larger α, with $\alpha > 10^3$, the growth of the separation depth is more gradual, revealing that separation and growth occur simultaneously. Presumably, even in this case the system will eventually reach a metastable state, but, due to computational limitations, we could not see it.

The behavior of a phase-separating system depends as much on the driving force $\mathbf{F}_\phi$ as on the Peclet number α. Consider, for example, the behavior of two systems with Peclet numbers $\alpha = 0$ and $\alpha = 10^3$. In Fig. 13 we see that, at time $\tau = 0.08$ and with the same $s = 0.6$, the system with $\alpha = 0$ is in a metastable state, while that with $\alpha = 10^3$ is still in the domain-forming, separating stage. In fact, although the capillary driving force $\mathbf{F}_\phi$ is the same in the two cases, since it is a function of the separation depth s, it can induce a strong convection only for systems

with small viscosities (i.e. with large α's), while for very viscous systems it has hardly any effect.

5.3 Off-critical Quenches

In Figure 14 we show the separation process for off-critical mixtures with $\phi_0 = 0.45$. As in the critical case, the system tends to form larger single-phase domains as the convection coefficients α increases. Again, while for smaller α the processes of separation and growth occur successively in time, for larger α they occur simultaneously. However, while for critical mixtures the separating phases tend to form interconnected domains, for off-critical mixtures we observe the formation of isolated, mostly circular drops, with no detectable double phase separation. The larger is α, the shorter is the relaxation time of a drop after a collision, so that for $\alpha > 10^2$ we practically do not observe any non-circular drops. As we see in Figure 15, compared to the critical case, the onset of phase separation for off-critical mixtures occurs at later times. In particular, the closer ϕ_0 is to the spinodal concentration ϕ_s (in our case, with $\Psi = 2.1$, $\phi_s = 0.388$), the longer it takes for the onset of phase separation. In addition, in off-critical mixtures the processes of separation and growth tend to occur successively in time, even at high values of the Peclet number. For example, comparing Figures 13 and 15, we see that for $\alpha = 10^3$, the two processes occur simultaneously in the critical case, and sequentially in the off-critical

one. That means that off-critical mixtures are more likely to reach a metastable state, after which single-phase domains grow much more slowly.

5.4 Temporal Growth the Domain Size

Finally, the equivalent average radius of the drops, R, is plotted in Figure 16 as a function of time. For a given value of $\alpha < 10^4$, the equivalent radius grows linearly with time, until it reaches a saturation value, corresponding to the above-mentioned metastable state, after which it grows more slowly. In particular, when $\alpha = 0$, metastable states grow like $t^{1/3}$. On the other hand, when $\alpha > 10^4$, the equivalent radius appears to grow linearly until it attains a value which is comparable to the size of the system. Again, when $\alpha = 10^4$, due to computational limitations, we could not see the size of the microdomains corresponding to a metastable state. The linear growth follows the curve $R \sim 10^3 a\tau = 10^{-2} Dt/a$, and appears to be independent of α. This scaling of the temporal growth dR/dt can be easily determined, considering that $dR/dt = |\mathbf{j}|/\rho$, where $\mathbf{j}$ is the mass flux at the interface, which, far from equilibrium, can be estimated as $|\mathbf{j}| \sim \rho(\Delta\phi)\left[2\phi(1-\phi)\Psi - 1\right](a/\ell)(D/a)$, with $\ell \sim a/\sqrt{\Psi - 2}$ denoting the characteristic thickness of the interface [14]. Therefore, considering that $(\Delta\phi) \sim \sqrt{\Psi - 2}$, we obtain:

$$\frac{dR}{dt} \sim \beta \frac{D}{a}, \tag{5.1}$$

where $\beta = (\Psi - 2)^2$. Note that for $D \sim 10^{-5} cm^2/s$ and $a \sim 10^{-5} cm$, we obtain: $dR/dt \sim 100\mu/s$, in excellent agreement with the experimental results [23].

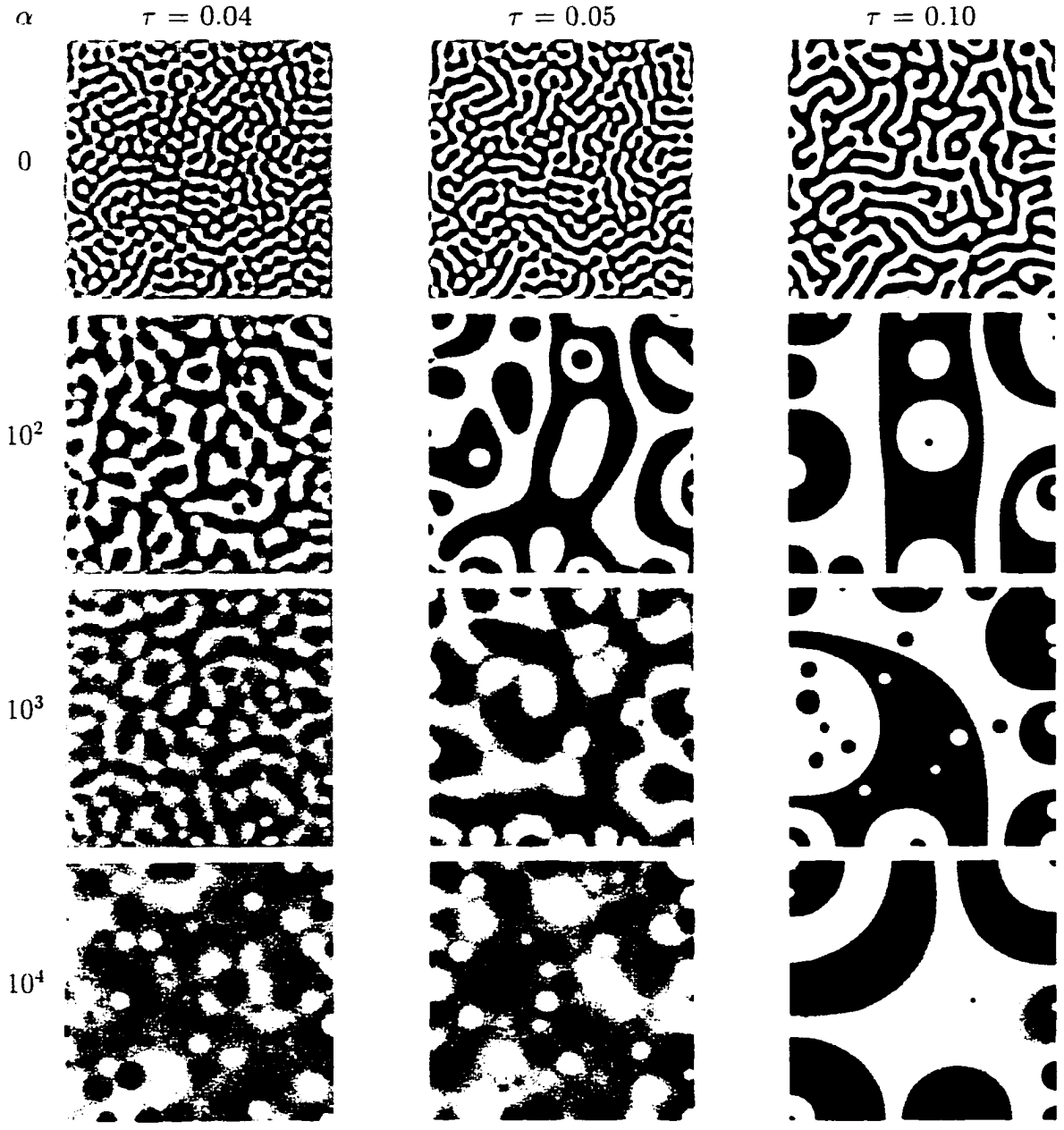

Figure 11. Composition of a binary mixture at different times τ after an instantaneous quenching with $\Psi = 2.1$ and $\phi_0 = 0.5$, when the Peclet number α is 0, 10^2, 10^3 and 10^4. The size of the system is $400a \times 400a$, with no flux boundary conditions. The snapshots correspond to $\tau = 0.04$, 0.05 and 0.10, expressed in $10^5 a^2/D$ units. The gray level varies linearly between black and white, corresponding to concentrations $\phi = \phi_{eq}^A$ and $\phi = \phi_{eq}^B$, respectively.

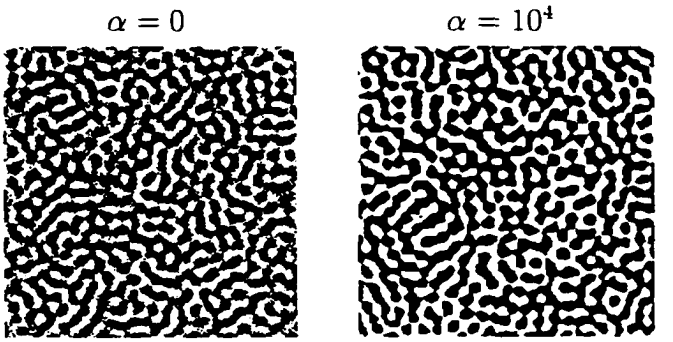

Figure 12. Concentration field after an instantaneous quenching with $\Psi = 2.1$ and $\phi_0 = 0.5$ at time $t = 0.02 \times 10^5 a^2/D$. when the Peclet number α is 0 and 10^4. The size of the system is $400a \times 400a$. with no flux boundary conditions. Black pixels correspond to concentrations $\phi < \phi_0$. and white ones to $\phi > \phi_0$.

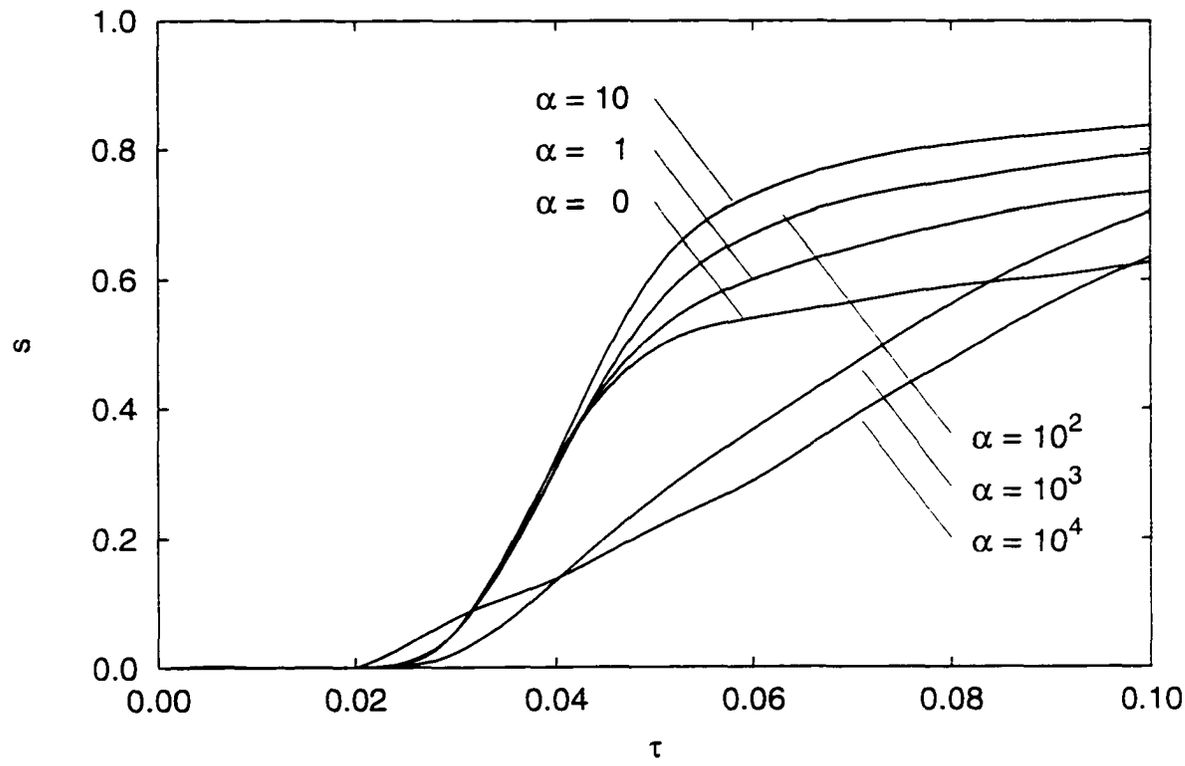

Figure 13. Separation depth s as a function of time τ for $\Psi = 2.1$. $\phi_0 = 0.5$. and with different values of the Peclet number α. Results were obtained using $1000a \times 1000a$ simulations.

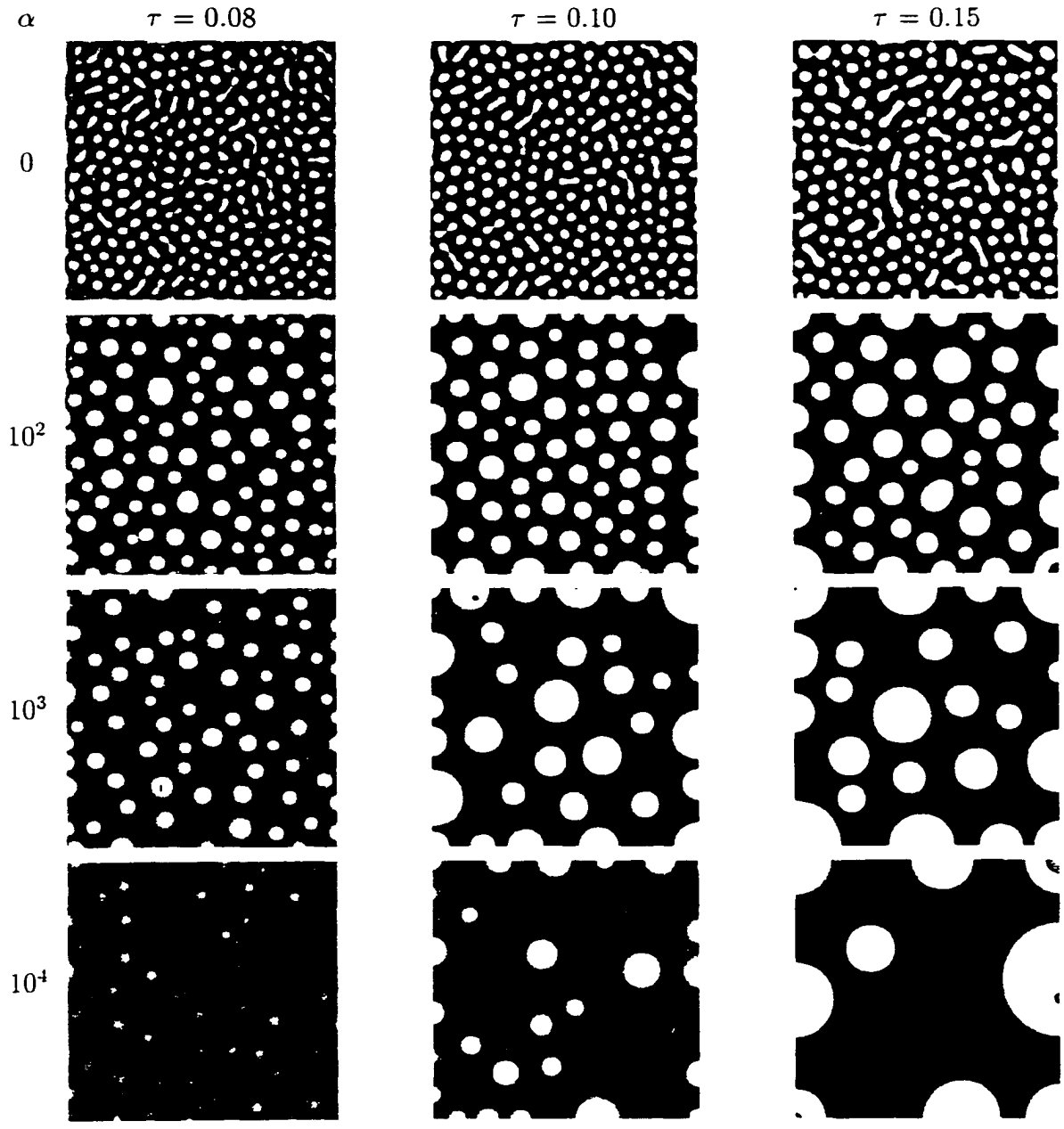

Figure 14. Composition of a binary mixture at different times τ after an instantaneous quenching with $\Psi = 2.1$ and $\phi_0 = 0.45$, when the Peclet number α is 0, 10^2, 10^3 and 10^4. The size of the system is $400a \times 400a$, with no flux boundary conditions. The snapshots correspond to times $\tau = 0.04$, 0.05 and 0.10, expressed in $10^5 a^2/D$ units. The gray level varies linearly between black and white, corresponding to concentrations $\phi = \phi_{eq}^A$ and $\phi = \phi_{eq}^B$, respectively.

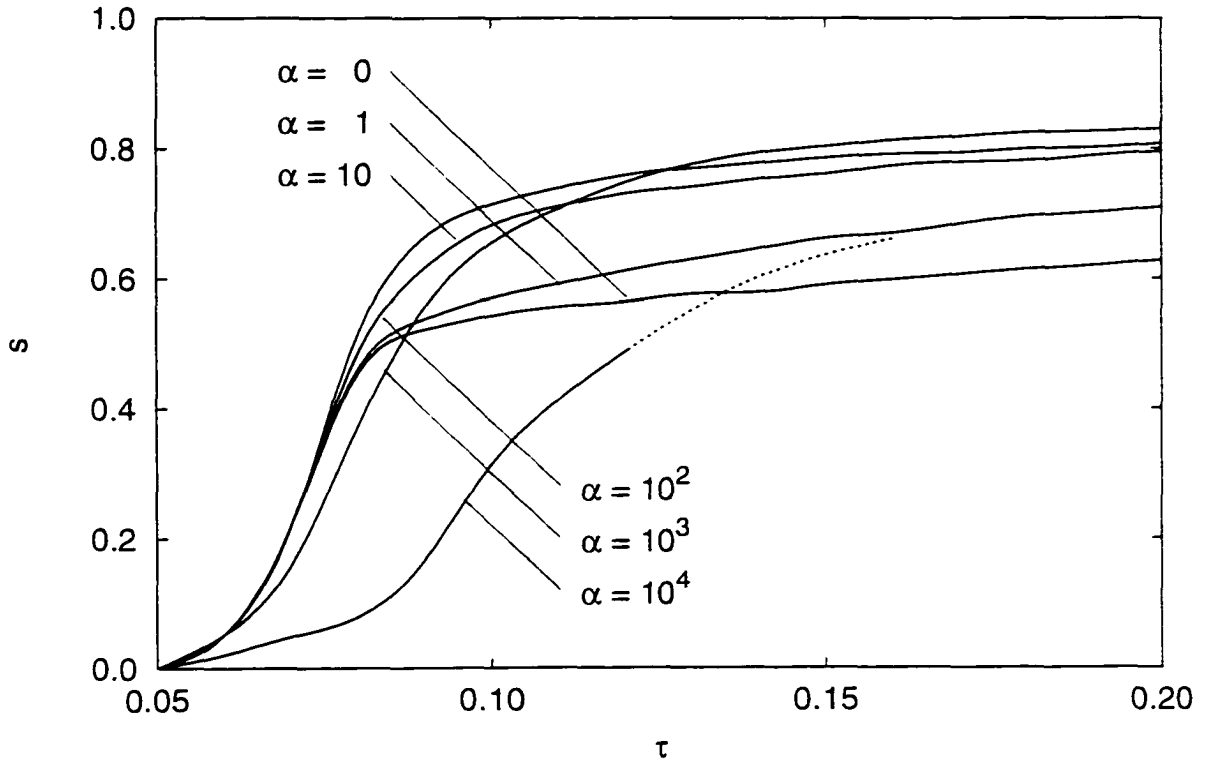

Figure 15. Separation depth s as a function of time τ for $\Psi = 2.1$, $\phi_0 = 0.45$, and with different values of the Peclet number α. Results were obtained using $1000a \times 1000a$ simulations.

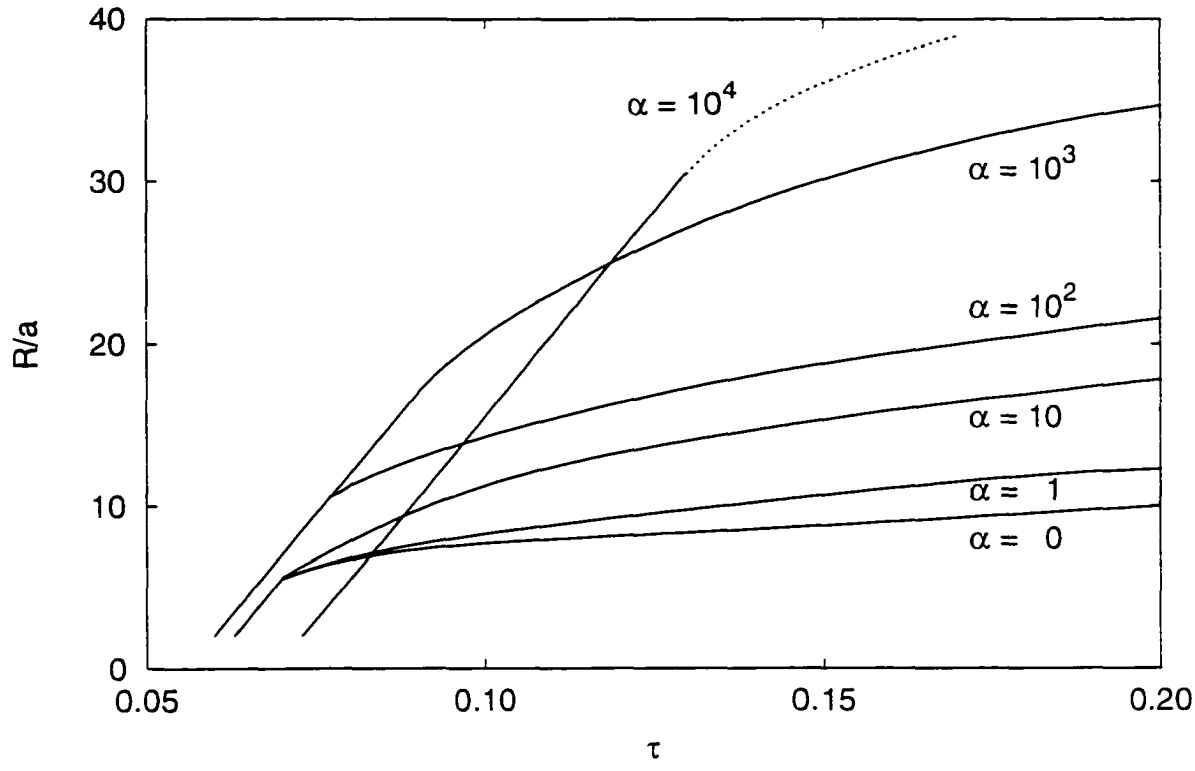

Figure 16. Equivalent average radius R as a function of time τ for $\Psi = 2.1$, $\phi_0 = 0.45$, and with different values of the Peclet number α. Results were obtained using $1000a \times 1000a$ simulations.

CHAPTER 6

MOTION OF DROPLETS DURING LATE STAGE OF PHASE SEPARATION

In this section we consider a well-separated system, that is a mixture composed of single-phase domains of uniform, but not necessarily equilibrium, concentration, separated by sharp interfaces. We discuss here simple models to study the motion for of single-phase droplets surrounded by the continuum phase, using numerical solutions of Equations (3.2)-(3.3) with initial conditions simulating isolated drops of A-rich phase immersed in a B-rich liquid.

6.1 Motion of a Single Drop in a Concentration Gradient

Consider an isothermal system composed of a drop with radius R and concentration ϕ_d, surrounded by a continuum phase with concentration $\phi_c = 1 - \phi_d$ and an imposed initial concentration gradient $\nabla\phi_c$. Since the width of the interface $\ell \approx a/\sqrt{\Psi - 2}$ is constant, while the concentration drop across the interface, $\Delta\phi = \phi_d - \phi_c$, is larger on one side of the drop than on the other (see Fig. 17), a surface energy difference between the front and the back of the drop will result [cf. Eq. (3.5)]. This surface energy gradient will induce a Marangoni force, which, in turn, leads to the motion of the drop. Concomitantly, the system is phase separating,

with the concentration of the drop and that of the continuum phase tending to their equilibrium values $(\phi_c)_{eq}$ and $(\phi_d)_{eq}$, respectively. Assuming that the mean particle velocity V is much larger than the typical growth rate of the drop, dR/dt, as it phase-separates, the concentration around the drop can be considered approximately equal to its unperturbed value (i.e. it varies linearly with position). Therefore, the energy integrated over the surface of the drop (in 3D) is equal to $E = 4\pi R^2\sigma$, where σ is the surface tension evaluated at the drop center. Consequently, imposing that the driving force $\mathbf{F} = \nabla E = 4\pi R^2\nabla\sigma$ is equal to the drag force $\mathbf{F} = -5\pi\eta R\mathbf{V}$, with $\mathbf{V}$ denoting the constant translational velocity, and where we have assumed that the drop and the surrounding liquid have the same viscosity η, we obtain,

$$\mathbf{V} = -\frac{4R}{5\eta}\nabla\sigma = -\frac{4}{5}\sqrt{\Psi - 2}(\Delta\phi)^2\alpha\left(\frac{D}{a}\right)R\frac{\nabla\sigma}{\sigma}.$$

Here $\alpha^{-1} = (M_W/\rho RT)(\eta D/a^2)$, defined in Eq. (3.4), represents the capillary number and the surface tension σ is given by Eq. (3.5), with $(\Delta\phi)$ denoting the mean concentration drop across the interface. Finally, using again Eq. (3.5), we find that $\nabla\sigma/\sigma = -4\nabla\phi_c/(\Delta\phi)$, and considering that $(\Delta\phi) \sim \sqrt{\Psi - 2}$, we obtain,

$$\mathbf{V} = K\,\alpha\left(\frac{D}{a}\right)R\nabla\phi_c. \tag{6.1}$$

with $K \sim (\Psi - 2)$.

As we mentioned above, the translational velocity must be compared with the temporal growth dR/dt, with $dR/dt \sim (\Psi - 2)^2 (D/a)$ [cf. Eq. (6.3)]. Therefore, as this analysis is valid only when $V \gg dR/dt$, we obtain the following inequality.

$$\frac{\alpha^{-1}(\Psi - 2)}{R\nabla\phi_c} \ll 1. \tag{6.2}$$

A similar treatment was presented by Karpov and Oxtoby [25]. Although this model is valid for 3D systems and uses rough approximations for both Marangoni's and drag forces, it describes qualitatively the velocity dependence on the concentration gradient and the capillary number. The dependence on the drop size is obviously a strong function of the dimensionality of the problem, as in 2D Stokes' paradox prevents us from evaluating the drag of the drop (in fact, it should be infinite).

The problem of this Section is somewhat similar to that studied by Subramanian [42], who generalized Young, Goldstein and Block's [43] results on thermocapillary motion to the case of a single drop, immersed in an immiscible background phase, while a solute, miscible in both phases, is diffusing within the whole domain, i.e. in and out of the drop. Assuming that the surface tension σ depends on the local solute concentration c, an imposed concentration gradient of the solute, $(\nabla c)_\infty$, would generate a Marangoni force, inducing the motion of the drop. Not surprisingly, in the dilute limit, $c \ll 1$, as the solute concentration c satisfies the heat equation, the migration velocity of the drop $\mathbf{V}$ is given by an expression similar to Young, Goldstein and Block's [43] thermocapillary velocity, i.e. [42], $\mathbf{V} \sim (\partial\sigma/\partial c)\eta^{-1}R(\nabla c)_\infty$. Clearly,

apart from a numerical coefficient, this formula is equivalent to Eq. (6.1), showing that the migration velocity is proportional to the concentration gradient and to the drop size, and is inversely proportional to the viscosity of the fluids (which means that it is proportional to the inverse capillary number α).

In our simulations, the drop has an initial radius $R_0 = 10a$, with average concentration $\phi_d = 0.55$ and is immersed in a concentration gradient of the continuum phase, $|\nabla\phi_c| = 10^{-4} - 10^{-3}a^{-1}$. As expected, since the inequality (6.2) is satisfied, we observe that the drop moves straight in the direction of $\nabla\phi_c$, with a speed that is proportional to $|\nabla\phi_c|$ and proportional to the inverse capillary number α^{-1} (see Fig. 18), in agreement with Eq. (6.1). However, comparing the results of Fig. 18 with the predictions of Eq. (6.1), we see that, instead of a slope $K \sim (\Psi - 2) \sim 10^{-1}$, we obtain $K \approx 0.04\,(R/a) \sim 4.\,10^{-3}$. As already mentioned, the smaller-than-expected absolute value of the velocity is probably related to the very large drag experienced by the 2D drop. The dependence of the translational velocity on the drop size is also more complicated than the simple linear relation predicted by Eq. (6.1): in fact, as shown in Fig. 19, it appears that $\mathbf{V}$ depends linearly on R only for small R's, or equivalently, for small concentration gradients, while for larger R's the velocity of the drop evens out, reaching a plateau. Similar results were obtained by Jasnow and Viñals [22], who applied the model H to study the thermocapillary migration of drops.

6.2 Motion of a Single Drop in a Uniform Concentration Field

Consider an isolated drop with uniform initial concentration $(\varphi_d)_0$ immersed in a concentration field with uniform initial concentration $(\varphi_c)_0 = 1 - (\varphi_d)_0$. Since the concentration of the drop and that of the continuum phase tend to their respective equilibrium value, the drop will absorb (or desorb) material from (or to) the background field. In doing so, the concentration profile around the drop will become non-uniform, thereby inducing a body force $\mathbf{F}_\varphi$ which may lead to the motion of the drop. Comparing Fig. 20 and Fig. 21, we see that the movement of the drop depends on whether the initial concentration depth $(\Delta\phi)_0 = (\varphi_c)_0 - (\varphi_c)_{eq}$ is > 0 or < 0. In the first case, the drop absorbs material from the surrounding continuum phase, digging a "ditch" all around its perimeter and inducing the capillary driving force $\mathbf{F}_\varphi$ which then leads to the motion of the drop. So, the drop motion is self-sustained: each drop generates a change of the surrounding continuum phase, which in turn induces a force which moves the drop. On the other hand, when $(\Delta\phi)_0 < 0$, the drop diffuses out and eventually disappears, without moving. Clearly, when $(\Delta\phi)_0 = 0$, the drop is at equilibrium with the background field and does neither move, nor change its size.

Note that, while a drop immersed in a concentration gradient moves even when its size remains constant, the motion of a drop immersed in a uniform concentration field with $(\Delta\phi)_0 > 0$ is intrinsically connected to its changing size, i.e. if the drop does not absorb material from the background field, it won't move. In Fig. 22

the drop radius is plotted as a function of time, showing that the growth rate dR/dt is constant, even in the case $(\Delta\phi)_0 = 0.315$, when the drop radius increases four times during the time interval considered. This has to be expected, considering that $dR/dt = |\mathbf{j}|/\rho$, where $\mathbf{j}$ is the mass flux at the interface, which, far from equilibrium, can be estimated as $|\mathbf{j}| \sim \rho(\Delta\phi)\left[2\phi(1-\phi)\Psi - 1\right](a/\ell)(D/a)$, with $\ell \sim a/\sqrt{\Psi - 2}$ denoting the characteristic thickness of the interface [14]. Therefore, considering that $(\Delta\phi) \sim \sqrt{\Psi - 2}$, we obtain:

$$\frac{dR}{dt} \sim \beta \frac{D}{a}. \tag{6.3}$$

where $\beta = (\Psi - 2)^2$. In our case, with $\Psi = 2.1$, we obtain: $\beta \sim 10^{-2} D/a$, in agreement with the results of our simulations (see Fig. 22), and confirming that the growth rate is independent of the drop radius.

In Fig. 23, the instantaneous velocity of the drop, $|V|$, with $(\Delta\phi)_0 > 0$, is plotted as a function of time, showing that it strongly fluctuates around its mean value $\bar{V}$. This, in turn, depends on the driving force, that is proportional to the concentration depth $(\Delta\phi)_0$ of the "ditch" that the drop "digs" all over its perimeter (see Fig 20). The dependence of $\bar{V}$ and dR/dt on $(\Delta\phi)_0$ is represented in Fig. 24, revealing that $dR/dt \ll \bar{V}$, with both quantities increasing with $(\Delta\phi)_0$, and going to zero for $(\Delta\phi)_0 \approx 0.01$. This latter result seems to indicate that when the initial concentration depth $(\Delta\phi)_0$ is very small, the system finds itself in a metastable state, from which it can evolve only in the presence of a finite disturbance.

Following the motion of the drop, as in Fig. 25, we see that its motion looks random. In fact, denoting by $\mathbf{r}(t)$ the position of the center of the drop at time t, with $\mathbf{r}(0) = 0$, we can define the effective diffusivity D^* as,

$$D^* = \frac{\left\langle [r(t)]^2 \right\rangle}{4t}.$$

In Fig. 26 the effective diffusivity is plotted, showing that it does tend to an $O(D)$ constant value for long times. The fact that a drop has a diffusivity which is of the same magnitude as that of its molecules is an astonishing result.

6.3 Motion of Two Drops in a Uniform Concentration Field

In the two previous simulations we saw that drops modify their surrounding continuum phase and then move accordingly, driven by a capillary force which is proportional to the concentration gradient. Therefore, when two drops are close enough that each modifies the concentration distribution of the continuum phase surrounding the other, we expect that the net effect will be a mutual attractive force. In other words, as an A-rich drop travels towards regions with higher concentration of A, growing in size and leaving behind tails of purified B-rich fluid, it will influence the motion of another A-rich drop. In general, this attractive force can be seen as an attempt of the system to minimize its interfacial area and, therefore, its free energy. This mechanism has been explained very well by Tanaka [41].

Our simulations revealed that, as in the case of a single drop, the behavior of the system is very different, depending on whether $(\Delta\phi)_0$ is positive or negative. In fact, as illustrated in the sketches of Fig. 27, as drops start to move towards each other, when $(\Delta\phi)_0 > 0$ the concentration profile tends to form a concentration barrier between them, screening their mutual attraction, while when $(\Delta\phi)_0 < 0$ the mutual attractive force is unchallenged. Consequently, when $(\Delta\phi)_0 > 0$, the two drops may or may not coalesce as they approach each other, while, when $(\Delta\phi)_0 < 0$, they always end up coalescing, as shown in Figs. 28 and 29, respectively. In these two figures we see that, despite few burst expressing singular behavior, our computer model seems adequate in describing the process of two drops merging into one.

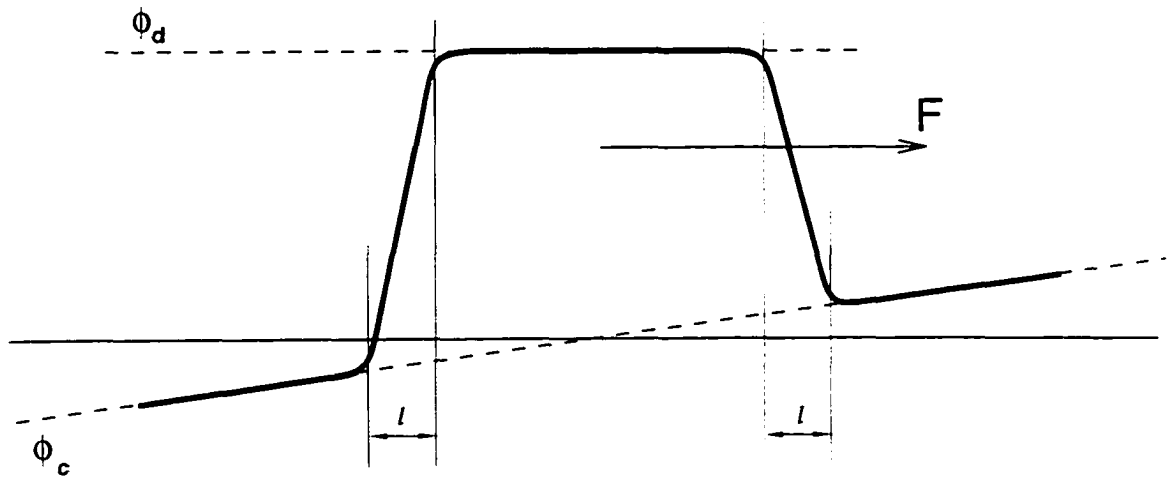

Figure 17. Isolated drop in a concentration field.

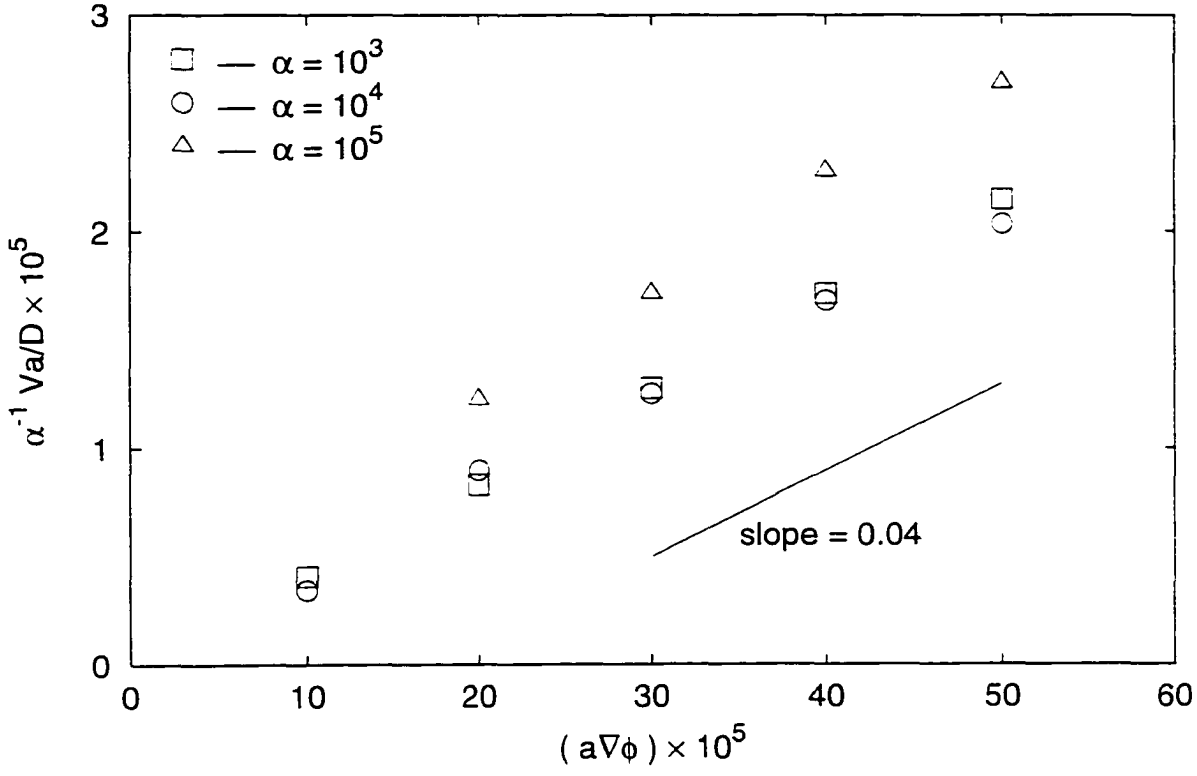

Figure 18. Velocity $\mathbf{V}$ of a drop with initial radius $R_0 = 10a$ as a function of the unperturbed concentration gradient $\nabla\phi_c$ in the continuum phase.

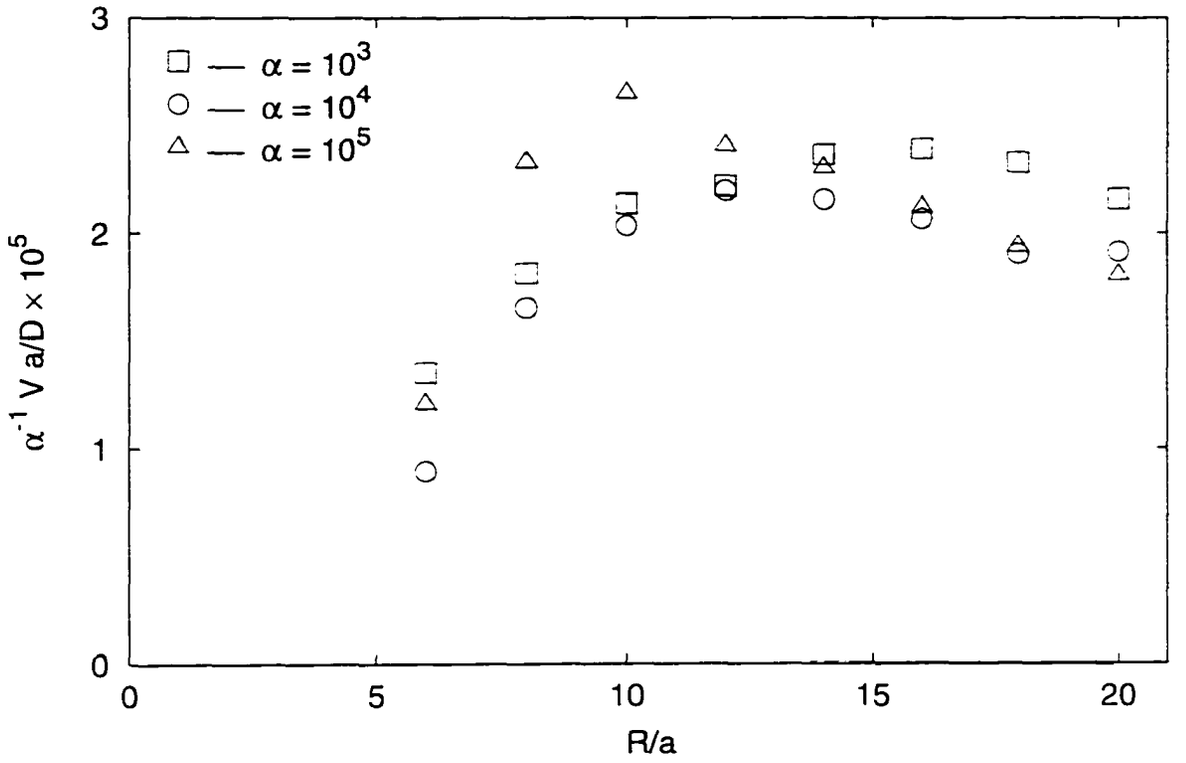

Figure 19. Velocity $\mathbf{V}$ of a drop with initial radius $R_0 = 10a$ as a function of its radius, for a given concentration gradient $\nabla\phi_c = 5.10^{-4}a^{-1}$ of the continuum phase.

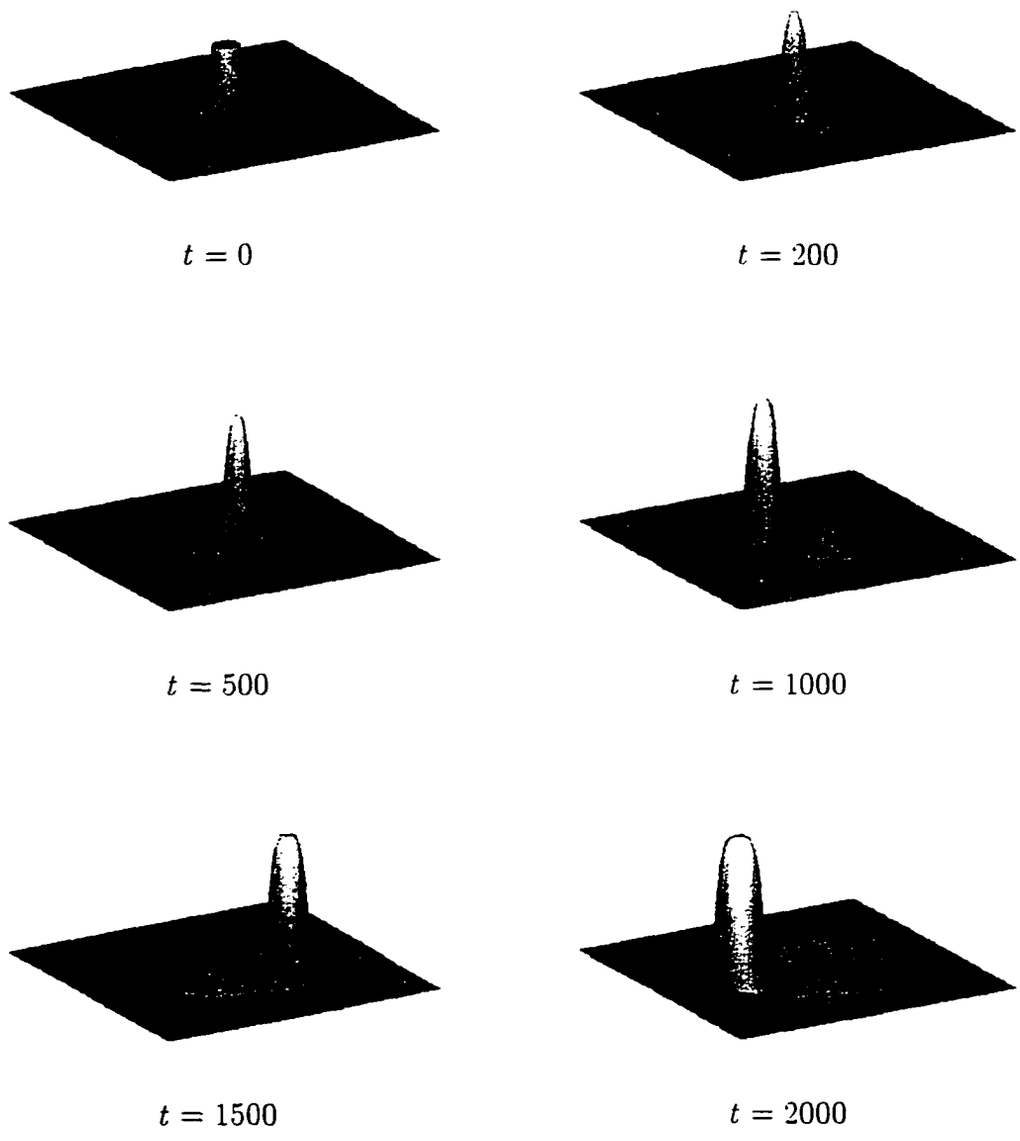

Figure 20. Evolution of the concentration field of a drop with initial radius $10a$. immersed in a continuum phase with $(\Delta\phi)_0 = 0.135$. The two-dimensional square grid has size $200a$ and time is given in a^2/D units.

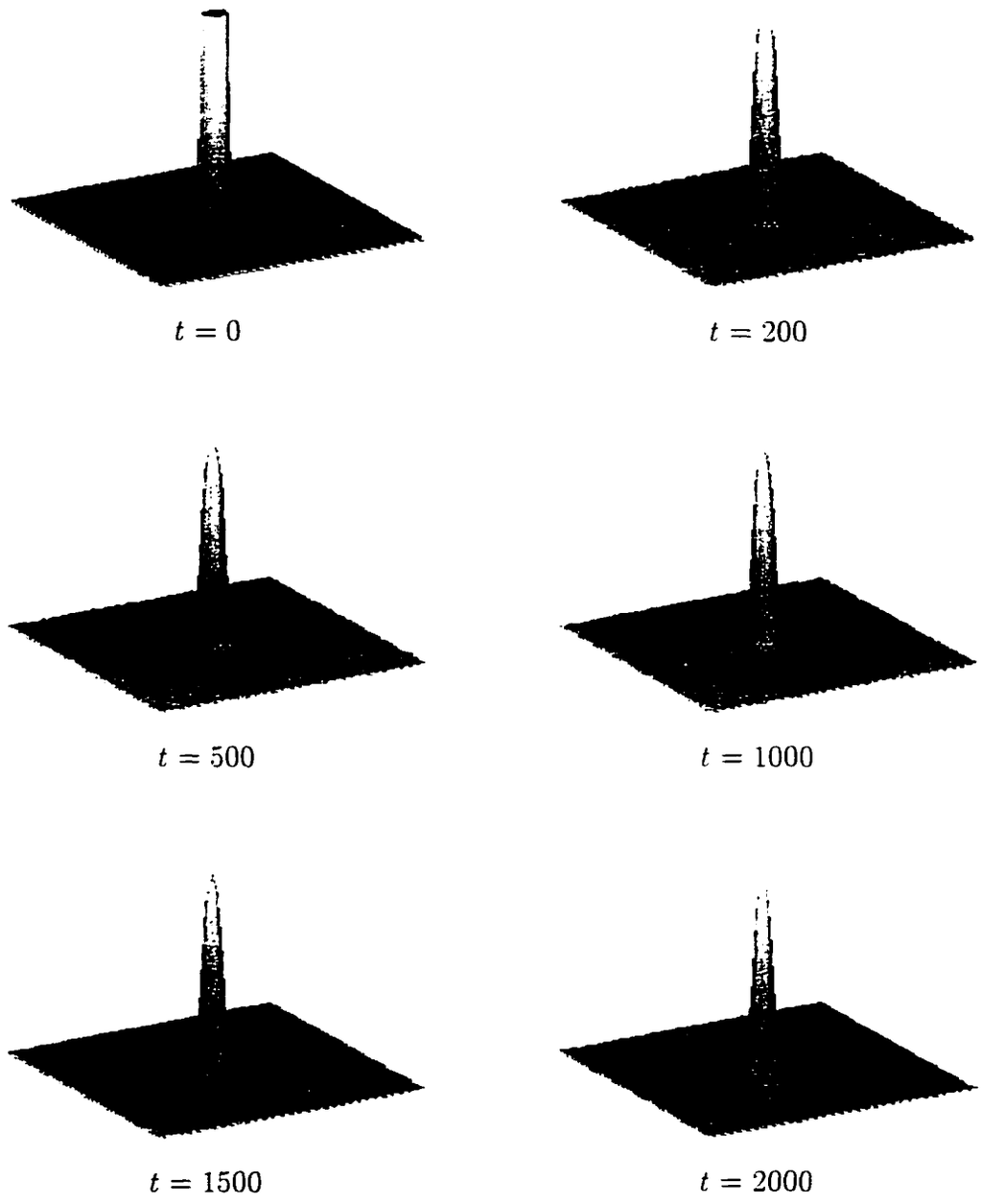

Figure 21. Evolution of the concentration field of a drop with initial radius $10a$. immersed in a continuum phase with $(\Delta\phi)_0 = -0.015$. The two-dimensional square grid has size $200a$ and time is given in a^2/D units.

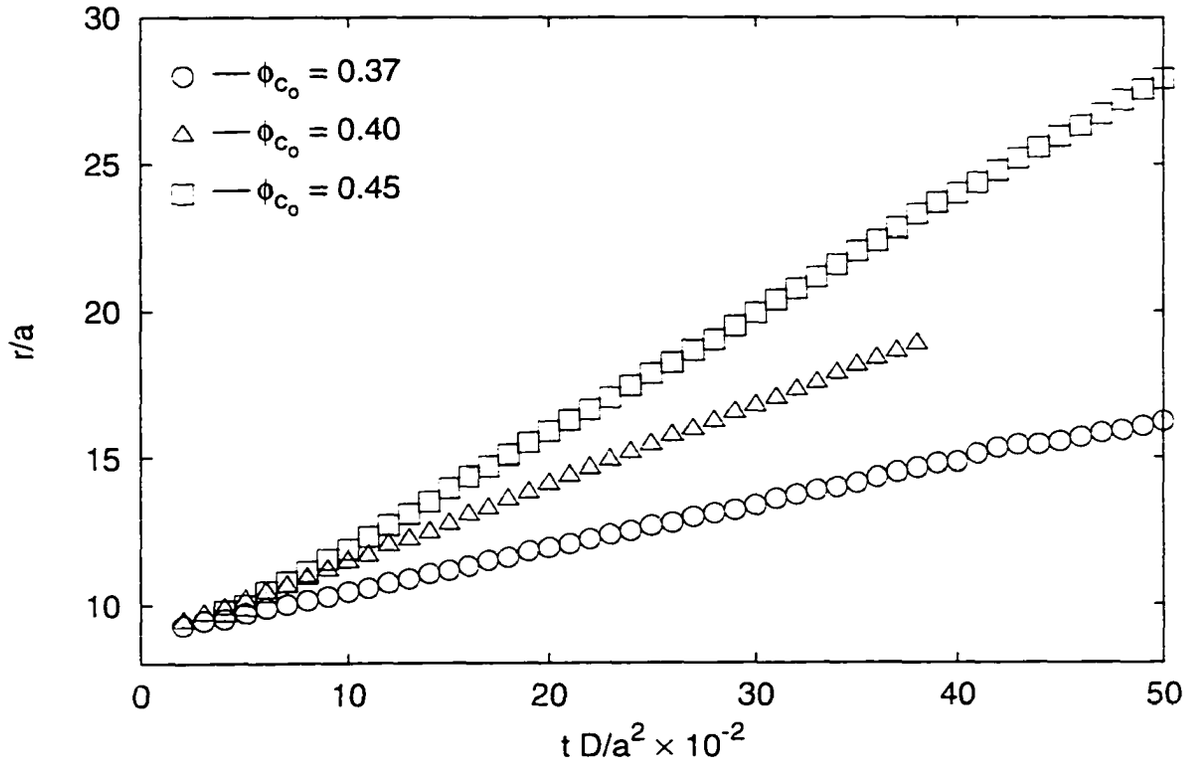

Figure 22. Radius of a phase-separating drop as a function of time. The drop, with initial radius $R_0 = 9.5a$, is immersed in a uniform concentration field with initial composition $(\phi_c)_o = 0.35$, 0.40 and 0.45, and with equilibrium composition $(\phi_c)_{eq} = 0.315$.

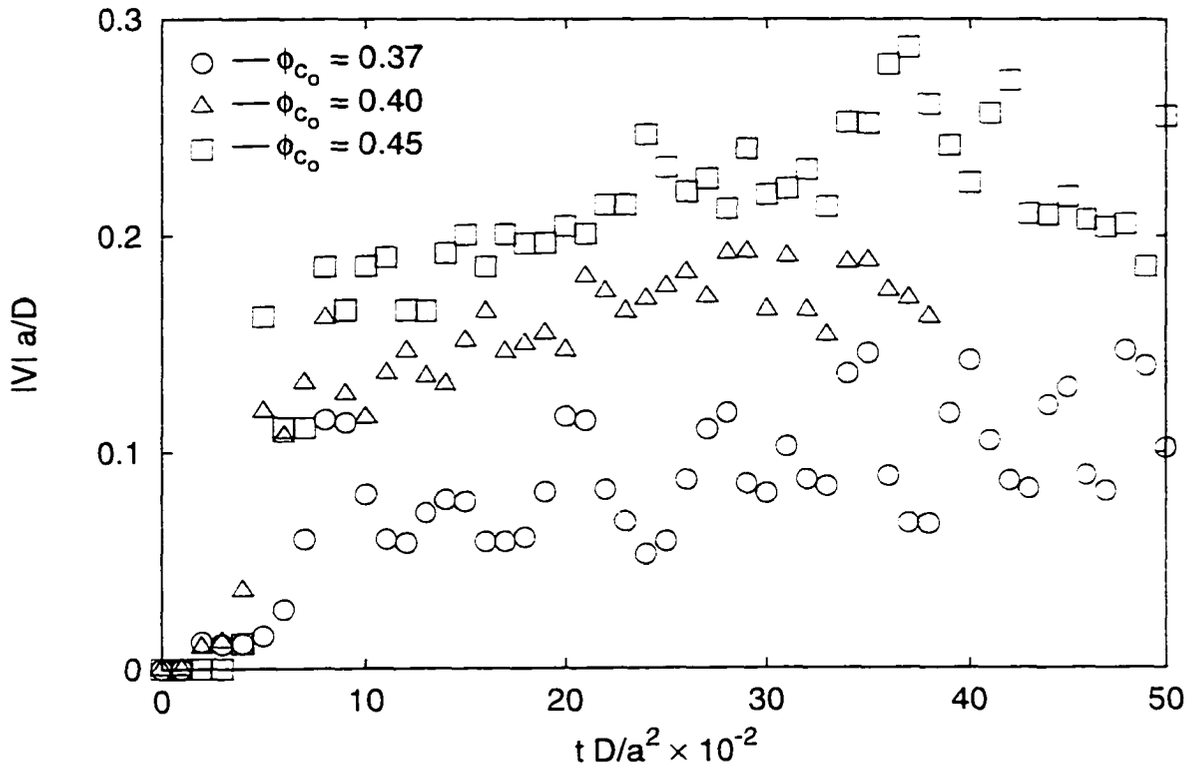

Figure 23. Instantaneous velocity $|V|$ of a phase-separating drop immersed in a uniform concentration field with initial composition $(\phi_c)_o = 0.35$, 0.40 and 0.45, and with equilibrium composition $(\phi_c)_{eq} = 0.315$.

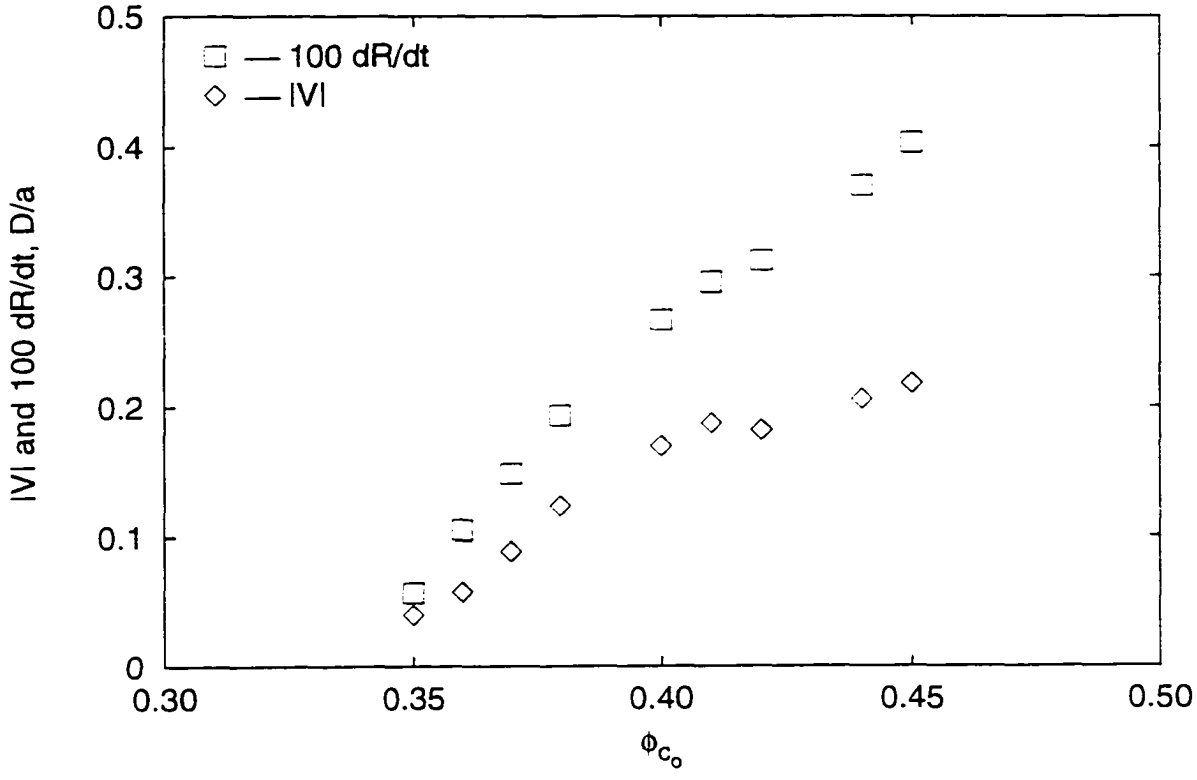

Figure 24. Mean velocity, $\bar{V}$, and growth rate dR/dt, as functions of the initial concentration depth $(\Delta\phi)_0$.

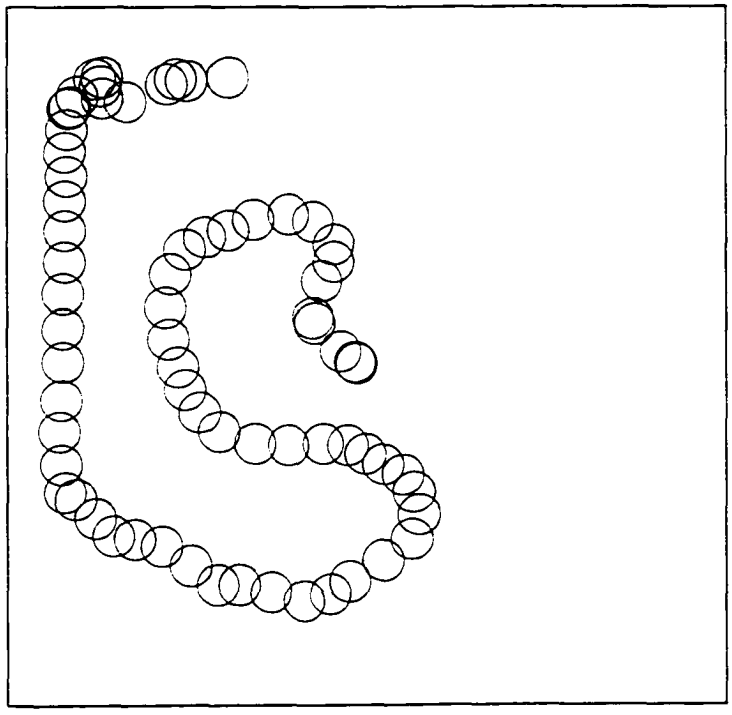

Figure 25. Trajectory of a drop with initial radius $R_0 = 9.5a$. immersed in a uniform continuum phase with initial composition $(\phi_c)_o = 0.45$ and inverse capillary number $\alpha = 10^4$. The position of the drop is shown at each time interval $\Delta t = 100a^2/D$: and the size of square grid is $400a$.

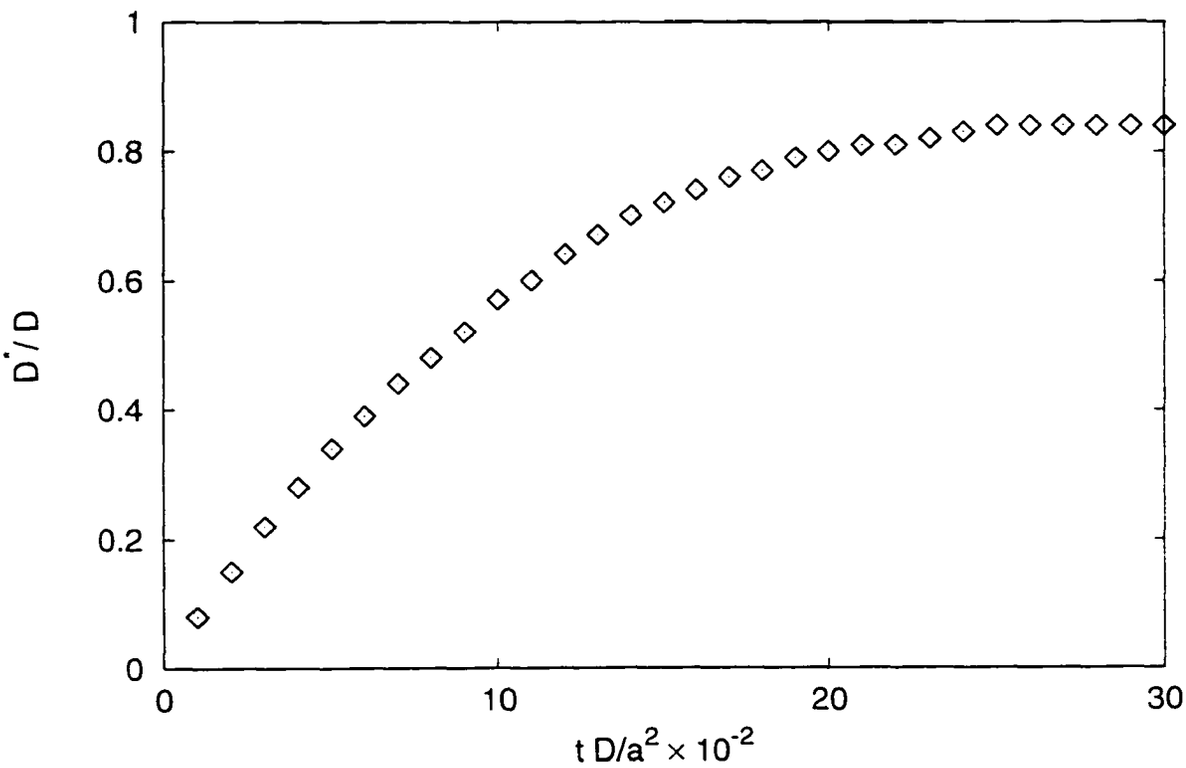

Figure 26. Effective diffusivity D^* of a drop with initial radius $R_0 = 9.5a$. immersed in a continuum phase with initial composition $(\varphi_c)_o = 0.40$ and inverse capillary number $\alpha = 10^4$.

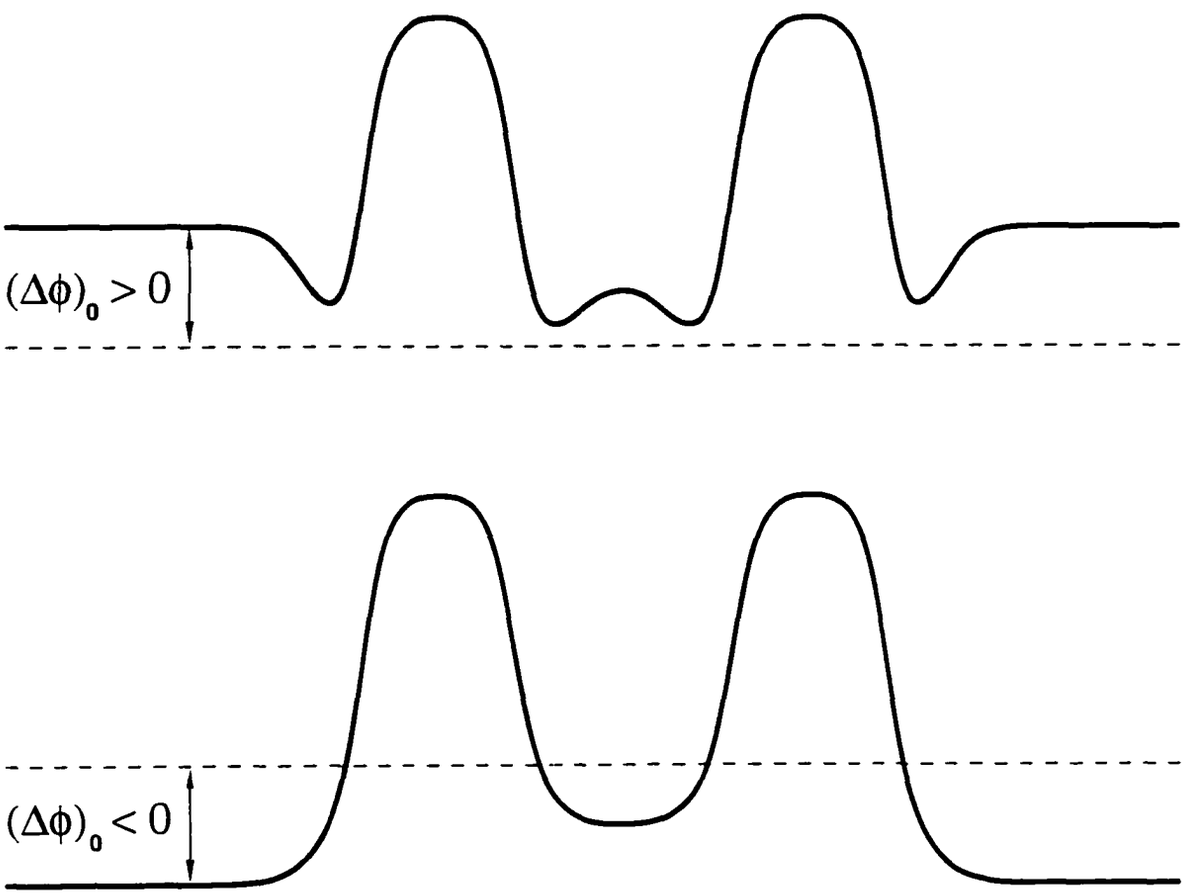

Figure 27. Sketches of the concentration profiles of two phase-separating drops when $(\Delta\phi)_0 > 0$ (top). and $(\Delta\phi)_0 < 0$ (bottom)

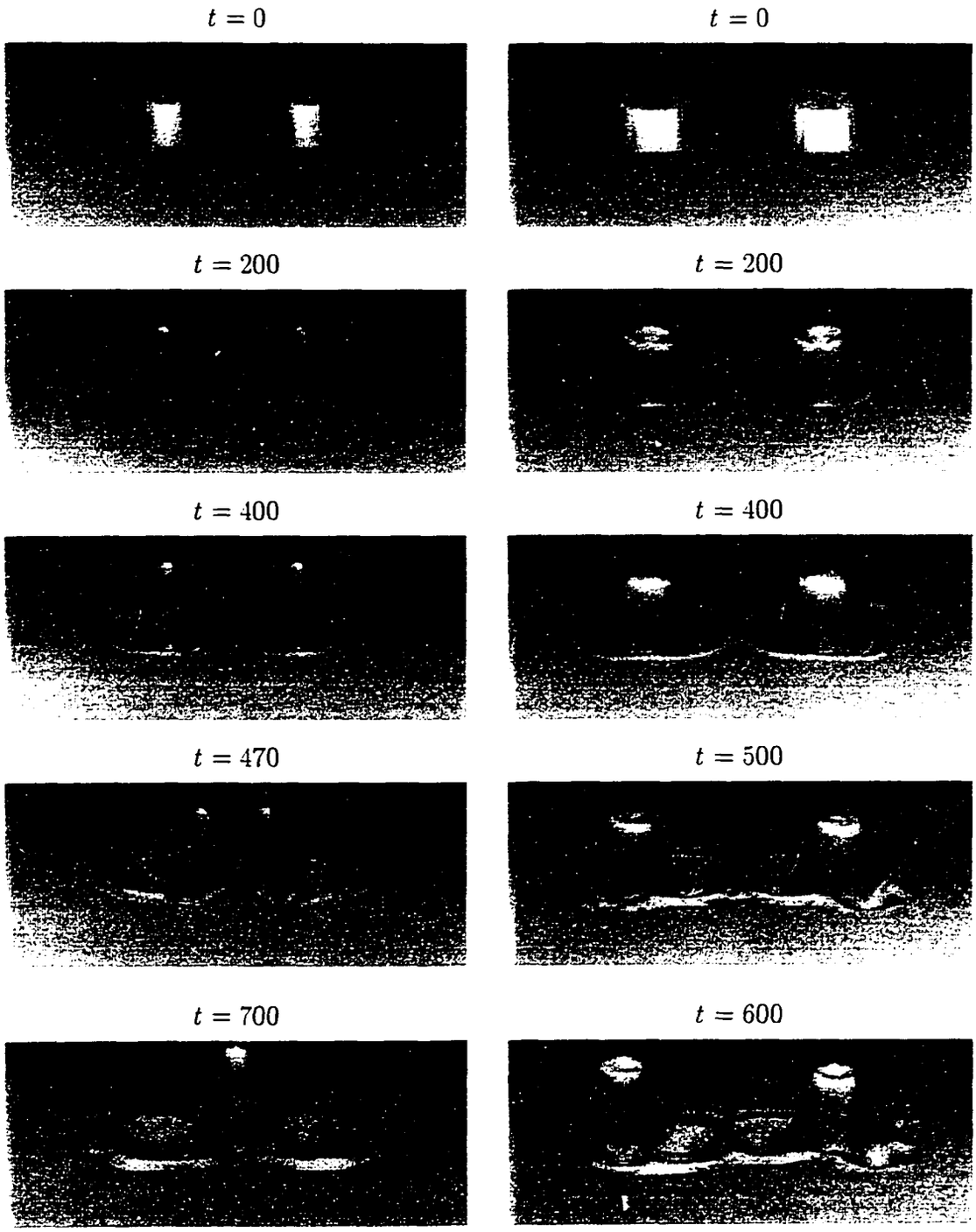

Figure 28. Evolution of the concentration field of two drops with initial radii $10a$ (left) and $16a$ (right), immersed in a continuum phase with $(\Delta\phi)_0 = 0.135$. The two-dimensional square grid has size $200a$. Time is given in a^2/D units.

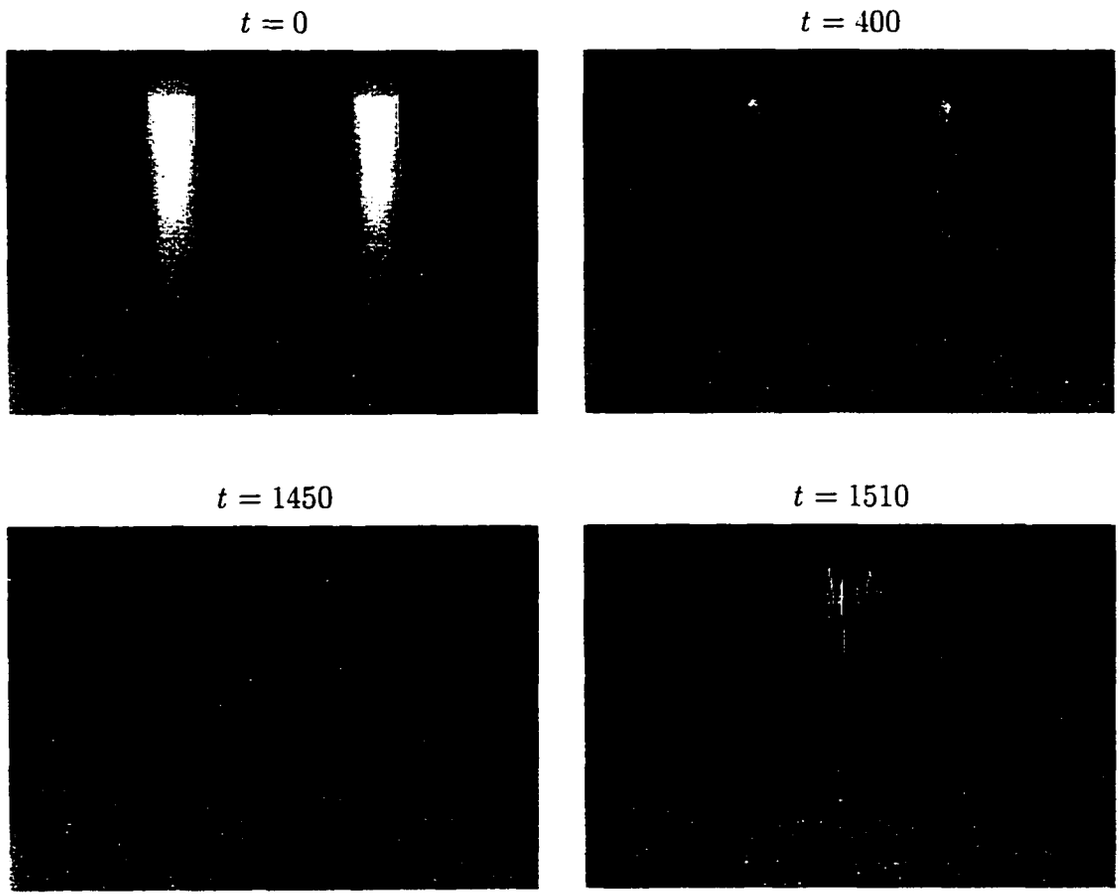

Figure 29. Evolution of the concentration field of the drop with initial radii $10a$. immersed in a continuum phase with $(\Delta\phi)_0 = -0.015$. The two-dimensional square grid has size $200a$. Time is given in a^2/D units.

CHAPTER 7
CONCLUSION

In this work, we study the phase separation of deeply quenched mixtures in which the diffusion coefficient depends on the local composition field ϕ. Our theoretical model follows the standard model H, where convection and diffusion are coupled via a body force, expressing the tendency of the demixing system to minimize its free energy. In the limit of sharp interfaces separating single-phase domains, this coupling term reduces to the capillary force. A simple dimensional analysis shows that this force depends on the Peclet number α, expressing here the ratio of thermal to viscous forces.

First, we consider the case of alloys and polymer melts with high viscosities, where $\alpha = 0$. We show that one-dimensional systems evolve until they reach a spatially periodic steady state, with a period that, for instant quenching, coincides with the wavelength of the mode of maximum growth of the linear stability analysis. Similar results are obtained also when the temperature of the system is the solution of the heat equation, but in this case the period of the periodic steady state solution increases as the heat diffusivity decreases. In 2D, the concentration profile, after reaching a periodic state similar to the 1D steady state, continues to evolve, forming single-phase domains separated by sharp interfaces, which then thicken as the system

tries to minimize its interfacial area. When the quench takes place across, or near, the critical point, the drops merge to form filaments which later coarsen and grow, while when the quench takes place far from the critical point and near the metastable region of the phase diagram, the length of these filaments decreases as the system becomes a collection of nucleating drops. The typical size R of these single-phase domains grow with time as $t^{1/3}$, in agreement with theoretical predictions. However, contrary to the the commonly accepted assumption of local equilibrium at the late stage of phase separation, the composition field within and without these microdomains is far from equilibrium even after the formation of sharp interfaces.

In liquid binary mixtures, where the Peclet number can be as high as $\alpha = 10^5$, phase separation is mostly driven by convection. Our simulations predict a linear growth rate $R \propto t$, with a growth rate proportional to the ratio between molecular diffusivity and interface thickness, in agreement with the experimental results. For small Peclet numbers, $\alpha < 10^2$, the formation of sharp interfaces and the growth of the single-phase domains are two stages of the process of phase segregation that occur successively to one another. On the other hand, for large Peclet numbers, $\alpha > 10^4$, phase separation and domain growth occur simultaneously.

Finally, the motion of liquid drops in phase-separated mixture is simulated in 2D. Three problems are considered. In the first, we study the motion of a single drop immersed in a continuum field with constant concentration gradient, finding that the drop speed is proportional to the concentration gradient and inversely pro-

portional to the capillary number. The second problem involves the motion of a single drop immersed in a homogeneous concentration field, when the difference $(\Delta\phi)_0$ between the initial concentration of the continuum phase and its equilibrium value is either negative or positive. In the first case, the drop shrinks without moving, while when $(\Delta\phi)_0 > 0$, the drop consumes material from the surrounding field and moves randomly, propelled by the induced capillary driving force. During its movement, the drop grows linearly in time, with a growth rate proportional to the ratio between molecular diffusivity and interface thickness. In addition, the random motion of the drop has an effective diffusivity which tends to a constant value, showing that the drop has a diffusivity which is of the same magnitude as that of its molecules. The third problem simulates the motion of two drops, showing that the capillary forces induce a mutual attraction between the two drops. When $(\Delta\phi)_0 < 0$, the attractive force is unchallenged, thus leading always to coalescence, while when $(\Delta\phi)_0 > 0$ a screening effect arises which may keep the two drops apart from each other.

REFERENCES

[1] P. DeBenedetti. *Metastable Liquid Concepts and Principles*. Ch. 3. Princeton University Press. Princeton. NJ (1996).

[2] J. Frenkel. *Kinetic Theory of Liquids*. Dover. New York (1946).

[3] Reviews on spinodal decomposition can be found in: P.C. Hohenberg and B.I. Halperin. *Rev. Mod. Phys.* **49**. 435 (1977); J.S. Langer. in *Systems Far from Equilibrium*. L. Garrido. ed... Lecture Notes on Physics No. 132. Springer Verlag. Berlin (1980); J.D. Gunton. M. San Miguel and P.S. Sahni. in *Phase Transition and Critical Phenomena*. Vol. 8. C. Domb and J.L. Lebowitz. eds.. Academic Press. London (1983).

[4] J.W. Cahn and J.E. Hilliard. *J. Chem. Phys.* **28**. 258 (1958); **31**. 688 (1959); J.W. Cahn. *J. Chem. Phys.* **30**. 1121 (1959); *Acta Metall.* **9**. 795 (1961).

[5] J.D. van der Waals. 1894. *Z. Phys. Chem.* **13**. 657. reprinted in *J. Stat. Phys.* **20**. 200 (1979).

[6] J.W. Cahn. *Acta Metall.* **14**. 1685 (1966); J.W. Cahn. *Trans. Metall. Soc. AIME* **242**. 166 (1968).

[7] S.W. Koch. R.C. Desai and F.F. Abraham. *Phys. Rev.* **A26**. 1015 (1982).

[8] See. for example. G.F. Mazenko and R.A. Wiskham. *Phys. Rev. E* **51**. 2886 (1995); A. Nakahara. T. Kawakatsu and K.Kawasaki. *J. Chem. Phys.* **99**. 9853 (1993); N. Akaiwa and P.W. Voorhees. *Phys. Rev. E* **49**. 3860 (1994); A. Chakrabarti. R. Toral and J.D. Gunton. *Phys. Rev. E* **47**. 3025 (1993).

[9] K. Binder. *Phys. Rev. A* **29**. 341 (1984); K. Binder. *Physica A* **140**. 35 (1986); W. Klein and C. Unger. *Phys. Rev. B* **28**. 445 (1983); C. Unger and W. Klein. *Phys. Rev. B* **29**. 2698 (1984).

[10] N.C. Wong and C. Knobler. *J. Chem. Phys.* **69**. 725 (1978); *Phys. Rev. A* **24**. 3205 (1981); E. Siebert and C. Knobler. *Phys. Rev. Lett.* **54**. 819 (1985).

[11] Y.C. Chou and W.I. Goldburg. *Phys. Rev. A* **20**. 2015 (1979); A.J. Schwartz. J.S. Huang and W.I. Goldburg. *J. Chem. Phys.* **62**. 1847 (1975); **63**. 599 (1975).

[12] P. Guenoun, R. Gastaud, F. Perrot and D. Beysens, *Phys. Rev. A* **36**, 4876 (1987); P. Guenoun, D. Beysens and M. Robert, *Phys. Rev. Lett.* **65**, 2406 (1990); D. Beysens, P. Guenoun, P. Sibille and A. Kumar, *Phys. Rev. E* **50**, 1299 (1994).

[13] E. Siggia, *Phys. Rev. A* **20**, 595 (1979).

[14] R. Mauri, R. Shinnar and G. Triantafyllou, *Phys. Rev. E* **53**, 2613 (1996).

[15] N. Vladimirova, A. Malagoi and R. Mauri, submitted to *Phys. Rev. E.*

[16] I.M. Lifshitz and V.V. Slyozov, *J. Phys. Chem. Solids* **19**, 35 (1961).

[17] T. Koga and K. Kawasaki, *Phys. Rev. A* **44**, R817 (1991), and references therein.

[18] J. E. Farrell and O.T. Valls, *Phys. Rev. B* ***40,*** 7027 (1989); *Phys. Rev. B* ***42,*** 2353 (1990); *Phys. Rev. B* ***43,*** 630 (1991).

[19] H. Tanaka and T. Araki, *Phys. Rev. Lett.* **81,** 389 (1998).

[20] P.C. Hohenberg and B.I. Halperin, *Rev. Mod. Phys.* **49**, 435 (1977);

[21] K. Kawasaki, *Ann. Phys. (N.Y.)* **61**, 1 (1970).

[22] D. Jasnow and J. Viñals, *Phys. Fluids* **8**, 660 (1996).

[23] R. Gupta, R. Mauri and R. Shinnar, submitted to *Phys. Rev. E.*, R. Gupta, R. Mauri and R. Shinnar, . *Ind. Eng. Chem. Res.* **35**, 2360 (1996)

[24] V.G. Karpov, *Phys. Rev. Lett.* **75**, 2702 (1995).

[25] V.G. Karpov and D.W. Oxtoby, *Phys. Rev. E* **55**, 7253 (1997).

[26] J.M. Prausnitz, R.N. Lichtenthaler and E. Gomes de Azevedo, *Molecular Thermodynamics of Fluid-Phase Equilibria*, 2nd ed., Prentice-Hall, New York (1986).

[27] P.G. deGennes, *J. Chem. Phys.* **72**, 4756 (1980).

[28] E.A. Guggenheim, *Mixtures*, Oxford University Press (1952).

[29] J.H. Hildebrand and S.E. Wood, *J. Chem. Phys.* **1**, 817 (1933).

[30] R.B. Bird, W.E. Stewart and E.N. Lightfoot, *Transport Phenomena*, Wiley, New York (1960).

[31] L. Landau and L. Lifshitz, *Fluid Mechanics*, Pergamon, New York (1953).

[32] S.R. De Groot and P. Mazur, *Non-Equilibrium Thermodynamics*, Dover, New York (1962).

[33] J.U. Brackbill, D.B. Kothe and C. Zemach, *J. Comput. Phys.* **100**, 335 (1992).

[34] P. Bjorstad, Ph.D. Dissertation, Stanford University (1980).

[35] T.M. Rogers, K.R. Elder and R.C. Desai, *Phys. Rev. B* **37**, 9638 (1988); K.R. Elder, T.M. Rogers and R.C. Desai, *Phys. Rev. B* **38**, 4725 (1988); T.M. Rogers and R.C. Desai, *Phys. Rev. B* **39**, 11956 (1989); K.R. Elder and R.C. Desai, *Phys. Rev. B* **40**, 243 (1989).

[36] H.-O. Carmesin, D.W. Heermann and K. Binder, *Z. Phys. B* **65**, 89 (1986).

[37] A. Cumming, P. Wiltzius, F.S. Bates and J.H. Rosedale, *Phys. Rev. A* **45**, 885 (1992).

[38] C. Sagui and R.C. Desai, *Phys. Rev. E* **49**, 2225 (1994).

[39] I.M. Lifshitz and V.V. Slyosov, *J. Phys. Chem. Solids* **19**, 35 (1961); C. Wagner, Z. Elektrochemie **65**, 581 (1961); E.D. Siggia, *Phys. Rev. A* **20**, 595 (1979); G.F. Mazenko, *Phys. Rev. E* **50**, 3485 (1994), and reference therein.

[40] R. Toral, A. Chakrabarti and J.D. Gunton, *Phys. Rev. B* **39**, 901 (1989).

[41] H. Tanaka, *Phys. Rev. E* **51**, 1313 (1995); *J. Chem. Phys.* **107**, 3734 (1997).

[42] R.S. Subramanian, *J. Fluid Mech.* **153**, 389 (1985).

[43] N.O. Young, J.S. Goldstein and M.J. Block, *J. Fluid Mech.* **6**, 350 (1959).

[44] W.R. White and P. Wiltzius, *Phys. Rev. Lett.* **75**, 3012 (1996).

[45] S. Walas, *Phase Equilibria in Chemical Engineering*, Butterworth, Boston (1985).

[46] M. Grant, M. San Miguel, J. Viñals and J.D. Gunton, *Phys. Rev. B* **31**, 3027 (1985).

IMAGE EVALUATION
TEST TARGET (QA-3)

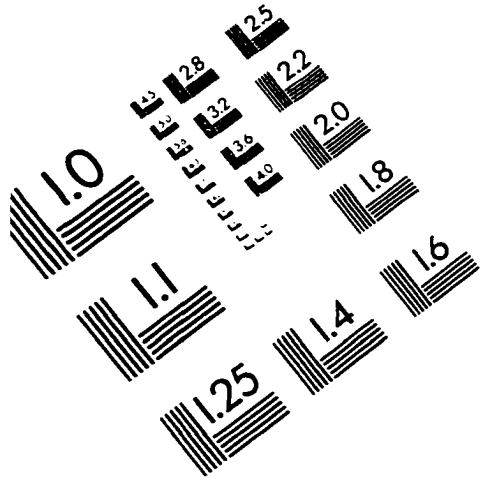

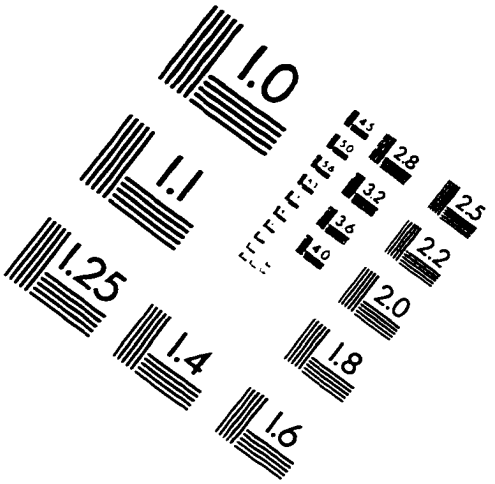

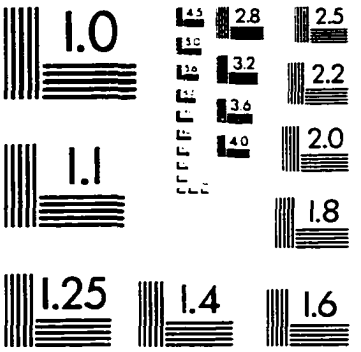

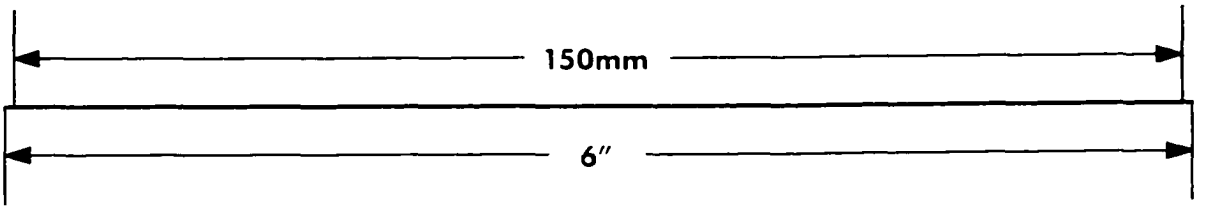

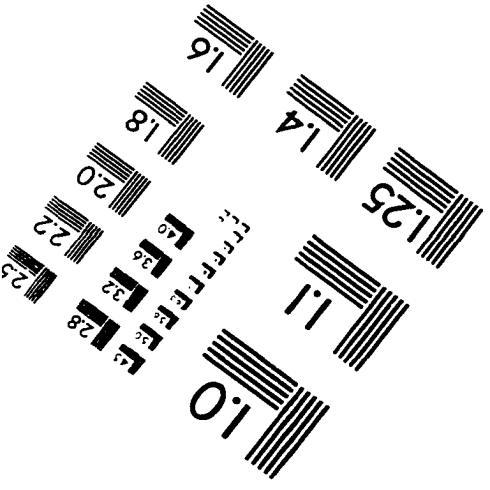

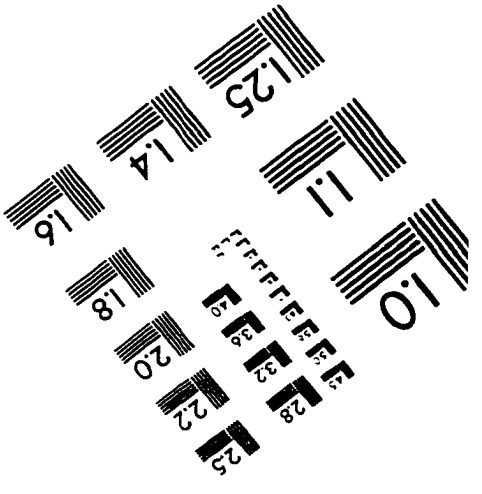

APPLIED IMAGE, Inc
1653 East Main Street
Rochester, NY 14609 USA
Phone: 716/482-0300
Fax: 716/288-5989